Simultaneous Optimization of Design and Operation of an Air-Cooled Geothermal ORC under Consideration of Multiple Operating Points

Marco Langiu[a,b], Manuel Dahmen[a], Alexander Mitsos[c,a,d,*]

[a] Forschungszentrum Jülich GmbH, Institute of Energy and Climate Research, Energy Systems Engineering (IEK-10), Jülich 52425, Germany

[b] RWTH Aachen University Aachen 52062, Germany

[c] JARA-ENERGY, Jülich 52425, Germany

[d] RWTH Aachen University, Process Systems Engineering (AVT.SVT), Aachen 52074, Germany

Abstract: We simultaneously optimize both the design and operation of an air-cooled geothermal organic Rankine cycle, maximizing total annual return (TAR), while considering multiple operating scenarios based on different ambient temperatures. In order to accurately capture realistic off-design behavior of the heat exchangers and turbine, as well as for the overall system, we incorporate component models that consider performance variations with both size and operating conditions. We employ a hybrid mechanistic data-driven modeling approach, involving artificial neural networks (ANNs) as surrogate models for accurate fluid properties, as well as for intermediate expressions for which ANNs improve tractability of the optimization problem. We demonstrate the importance of considering multiple operating conditions within design problems and propose a methodology for formulating and solving such problems globally, using our open-source solver MAiNGO.

1 Introduction

Organic Rankine cycles (ORCs) are an established technology for the conversion of heat to electricity, with geothermal applications constituting around three quarters of installed ORC capacity worldwide (Tartière and Astolfi, 2017). For a recent review of geothermal energy systems in general see, e.g., Lee et al. (2019). Due to their high availability, geothermal ORC systems can serve as a clean and renewable base load technology with the possibility for a high degree of autonomy (Kaplan et al., 1999; Kyriakarakos et al., 2020), with system capacities ranging from a few kW to several MW (Macchi and Astolfi, 2017b; Tartière and Astolfi, 2017). For inlet temperatures of the geothermal brine below 180 °C ORCs are economically preferable to dry or flash steam cycles (Nazif, 2011).

In regions where cooling water is not available, an air-cooled condenser (ACC) is the only option for heat rejection, making them a common choice for geothermal applications (Macchi and Astolfi, 2017b). As the heat transfer coefficient for air is low, large exchanger areas are needed, making ACC costs a major fraction of overall equipment costs (Mines and Wendt, 2013). In addition to ACC size, ambient temperature is another factor affecting cooling capacity, and parasitic losses of the ACC, and thus overall cycle efficiency. As a result, an optimal tradeoff between low investment costs and low parasitic losses in different operating conditions is crucial for a technically and economically viable system.

A large body of literature exists for optimization of ORCs in various fields of application, with focus on many different aspects, such as

- selection of optimal working fluids (e.g. Macchi, 2013; Lampe et al., 2014; Schilling et al., 2015, 2017) or working fluid mixtures (e.g., Huster et al., 2020b),
- turbine design (e.g., Macchi and Perdichizzi, 1981; Lazzaretto and Manente, 2014; Casartelli et al., 2015; Meroni et al., 2016; Seta et al., 2016) or heat exchangers (e.g., Pierobon et al., 2013; El-Emam and Dincer, 2013; Erdogan et al., 2017; Astolfi et al., 2017),
- superstructure optimization (e.g., Kalikatzarakis and Frangopoulos, 2016; Huster et al., 2020a).

For preliminary design optimization, system operation is commonly represented by a single operating point, e.g., Astolfi et al. (2014a,b) perform thermodynamic and thermoeconomic optimizations of an air-cooled ORC system for different cycle configurations, fluids, brine temperatures but consider a single fixed ambient temperature of 15 °C. To en-

* Alexander Mitsos,
E-mail: amitsos@alum.mit.edu

sure reliable performance, it is important that such preliminary optimizations are followed by so-called off-design analyses, where the operation under conditions other than the design point is considered. For a review considering small- to medium-scale applications see Liu et al. (2018). These off-design analyses may again leverage optimization; often this is done via operational optimizations which seek optimal operating strategies for a fixed design at different operating conditions. For instance, Manente et al. (2013) investigate off-design control strategies for an air-cooled ORC, maximizing net power for variations of ambient and brine temperatures from the values assumed during the design phase. However, generalizations of conclusions from such off-design analyses to other systems must be done with care. An example is the frequently stated observation that superheating results in reduced thermodynamic performance for subcritical cycles and that the use of a superheater is of little use or even detrimental (e.g., Saleh et al., 2007; Mago et al., 2008; Astolfi et al., 2014b; Song et al., 2020). Other design assumptions or operating conditions can however yield contradicting results, e.g., Ghasemi et al. (2013c,a) demonstrated that considering the off-design performance for an ORC using isobutane, superheat is valuable at high ambient temperatures. To obtain an overall optimum for a particular system, it is thus important to consider the effect of off-design explicitly during the design phase. A common approach for this is to repeatedly run a simulation model and select the design yielding the best results. Calise et al. (2014) perform multiple simulations of a solarthermal ORC at fixed design conditions, varying geometries of the heat exchangers. After determining the geometry that minimizes system costs they perform a second set of simulations to determine performance in off-design conditions. Similarly, Gómez-Aláez et al. (2017) consider an ORC recovering waste heat from hot flue gases of a gas turbine in a gas pipeline recompression station. They obtain a design point by fixing flue gas mass flow rate and temperature to their annual mean and maximizing net power. Subsequently they simulate off-design behavior, keeping turbine reduced mass flow and heat exchanger areas constant. In such simulation-based optimization approaches, all degrees of freedom must be pre-specified by appropriate assumptions or user inputs, hence the resulting designs are only optimal among the finite number of designs corresponding to the considered inputs.

An alternative approach is to let an optimization algorithm determine the optimal values for the degrees of freedom and other variables. For this, several works employ two-step approaches, first optimizing the system at design conditions, and subsequently with the obtained design at multiple off-design conditions. To avoid selecting a design that is suboptimal, such approaches are commonly iterated in different ways. Nusiaputra et al. (2014) devise a modular ORC for operation in different wellhead and ambient conditions and develop a control strategy under the assumption of fixed nominal net power and exergy input. In the first phase, component sizes and a design point are calculated based on fixed wellhead and ambient temperature. In the second phase, turbine nozzle opening, pump speed, and fan speed are varied for different off-design conditions via an evolutionary algorithm. The two phases are repeated for a grid of design conditions and the design point yielding the best results is selected as the optimum. The procedure is applied to three different climate regions and specific investment costs or mean cash flow are used as the selection criteria. Similarly, Capra and Martelli (2015) extend their previous work (Martelli et al., 2015) to include the consideration of part-load operation during the design of an ORC for a combined heat and power application. The authors employ a sequential quadratic programming (SQP) algorithm to optimize part-load in various operating conditions for fixed designs and a derivative-free black-box algorithm (Martelli and Amaldi, 2014) to search for better designs. Kalikatzarakis and Frangopoulos (2016) consider an ORC recovering waste heat at different operating conditions of a marine diesel engine and additionally include the system synthesis in the optimization. The optimization is based on a genetic algorithm which switches to an SQP algorithm when progress stagnates. Pili et al. (2019c) consider an air-cooled ORC for waste heat recovery from a steel billet reheating furnace with variations in the mass flow and temperature of the heat source, and the ambient temperature. In addition to the typical two phases of design and off-design under quasi-steady state conditions, results from the off-design optimizations are interpolated and used as setpoints in a dynamic simulation considering the inertia of the heat exchangers. In this way, a more detailed performance evaluation over the entire operating profile becomes possible.

All of the mentioned two-phase approaches have in common that some aspects of the system model are kept hidden from the optimizer and are only used for subsequent evaluation. As a consequence, the design found by these approaches may not be

optimal for the overall problem of design and operation. An alternative is to employ a mathematical programming model, which incorporates both system design and operation, and to give the optimizer access to all model equations. An early example of this approach is given in Yunt et al. (2008), where the design and operation of man-portable power generation systems is considered, and the equivalence of the resulting problem structure to stochastic programming problems (Birge and Louveaux, 2011; Kall and Wallace, 1994) is discussed.

The present work applies such a stochastic programming formulation to simultaneously optimize the design and operation of an air-cooled geothermal ORC. Based on flexible component models, which incorporate the effects of size and operating condition on efficiency and cost, we formulate and solve optimization problems that maximize expected total annualized return (TAR) for different sets of operating scenarios, represented by one or more ambient temperatures. Through the use of artificial neural networks (ANNs) as surrogate models, we incorporate detailed fluid properties and component characteristics while maintaining computational tractability. In Section 2 we present the models for the ORC system and its components, and our approach for quickly generating ANN surrogate models from data. In Section 3 we present computational results and Section 4 concludes this work.

2 Models and Methods

We consider the maximization of total annual return (TAR), calculated as

$$\mathrm{TAR} = -(1 + F_{\mathrm{op}})\, F_{\mathrm{ann}}\, C_{\mathrm{I,tot}} + C_{\mathrm{el}}\, \overline{P}_{\mathrm{net}}\, \tau_{\mathrm{op}}. \quad (1)$$

The first term corresponds to annualized capital expenses, where $C_{\mathrm{I,tot}}$ are the the total investment costs and we assume an operational cost factor $F_{\mathrm{op}} = 0.06$, a project lifetime of 20 years and a discount rate of 6%, resulting in an annuity factor of $F_{\mathrm{ann}} = 0.0871\,\frac{1}{\mathrm{a}}$. The second term is the revenue from electricity production with an assumed electricity price $C_{\mathrm{el}} = 80\,\frac{\mathrm{US\$}}{\mathrm{MW\,h}}$, the annual weighted average power production $\overline{P}_{\mathrm{net}}$ and the annual operating time $\tau_{\mathrm{op}} = 8000\,\frac{\mathrm{h}}{\mathrm{a}}$.

The total investment costs $C_{\mathrm{I,tot}}$ are

$$C_{\mathrm{I,tot}} = C_{\mathrm{I,E\&D}} + (1 + F_{\mathrm{BOP}}) \sum_{\mathrm{c} \in \mathcal{C}} C_{\mathrm{I,c}} \quad (2)$$

where $C_{\mathrm{I,E\&D}}$ are investments for exploration and development of the geothermal resource, assumed to be $15{\times}10^6$ US\$, $\mathcal{C}$ is the set of installed components (turbines, heat exchangers, pumps, etc.) and the coefficient $F_{\mathrm{BOP}} = 0.3$ takes into account balance of plant costs (Macchi and Astolfi, 2017b). Details on the investment costs for individual components, $C_{\mathrm{I,c}}$, will be given in the following sections. We point out that the assumed cost data are only given for replicability: they affect the numerical results, but not the proposed methodology, which is the focus of this work.

For a finite set of operating scenarios Ξ, with assumed relative likelihoods π^ξ, $\xi \in \Xi$, $\overline{P}_{\mathrm{net}}$ can be expressed as

$$\overline{P}_{\mathrm{net}} = \sum_{\xi \in \Xi} \pi^\xi\, P^\xi_{\mathrm{net}}, \quad (3)$$

where P^ξ_{net} is the net power for steady state operation in operational scenario ξ. Note that while dynamic effects play a crucial role for system control, quasi-steady state models as employed here are sufficiently accurate for techno-economic optimization as shown, e.g., by Pili et al. (2019a).

The system we consider is adapted from Ghasemi et al. (2013a). General assumptions are:

- A constant mass flow of $\dot{m}_{\mathrm{br}} = 660\,\frac{\mathrm{kg}}{\mathrm{s}}$ of geothermal brine (an aqueous solution of various minerals) with an initial temperature of $T_{\mathrm{br,i}} = 135\,^\circ\mathrm{C}$ and a pressure of $p_{\mathrm{br}} = 897\,\mathrm{kPa}$ is available.
- The minimum reinjection temperature is $T_{\mathrm{br,o,min}} = 60\,^\circ\mathrm{C}$ and the specific heat capacity is assumed to be constant, $c_{p,\mathrm{br}} = 4.1\,\frac{\mathrm{kJ}}{\mathrm{kg\,K}}$.
- The cycle to be considered is subcritical, recuperated, and uses the dry working fluid isobutane.
- Before expansion, the working fluid mass flow is split equally between two identical groups of turbines, recuperators and ACC banks.
- A direct ACC is employed, i.e., the working fluid is cooled via an air flow over finned condenser pipes, driven by a series of fans.
- In contrast to Ghasemi et al. (2013a), we consider a dedicated heat exchanger for superheating, and a single row of fans in each ACC bank instead of three. Additionally we only consider a single working fluid pump instead of three parallel ones, as power consumption of pumps – and thus their investment costs – are minor for subcritical cycles, see e.g., Huster et al. (2020a). Consequently modeling multiple pumps is expected to have little effect on the TAR.

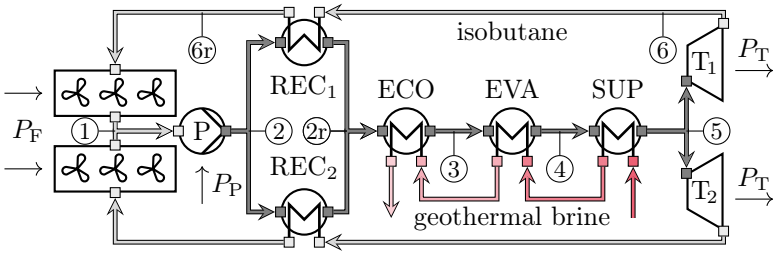

Fig. 1. Schematic of the considered ORC process. The working fluid isobutane is pressurized in a pump (P) requiring power P_P, split evenly, and preheated on the shell side of two recuperators (REC). The two streams are again mixed and heated, evaporated, and superheated on the shell side of an economizer (ECO), evaporator (EVA) and superheater (SUP), respectively, via geothermal brine. The working fluid is split again and expanded in two turbines (T), each producing power P_T, followed by heat recuperation. Finally it is desuperheated and condensed back to its original state in air cooled condenser, using electrically powered Fans (F), requiring a total power P_F.

- Pressure drops for the working fluid are negligible, which means there are only two pressure levels.

The resulting system structure is depicted in Fig. 1. With the above assumptions, the net electric power in each operating scenario is

$$P_\mathrm{net} = 2\,P_\mathrm{T} - n_\mathrm{F}\,P_\mathrm{F} - P_\mathrm{P}, \tag{4}$$

where the subscripts T, F, and P identify turbine, ACC fans, and pump, respectively, and n_F is the total number of fans. The nominal power for each of these components must be an upper bound to all occurring power levels:

$$P_\mathrm{c,nom} \geq P_\mathrm{c}^\xi \quad \forall \xi \in \Xi, \quad \forall \mathrm{c} \in \{\mathrm{T},\,\mathrm{F},\,\mathrm{P}\} \tag{5}$$

Together with these nominal values, the system design is specified via the heat exchanger geometries, the maximum pressure, the design enthalpy drop of the turbine and the design volumetric flow rate at its outlet, see the top of Tab. 1. System operation in each considered operating scenario is determined by the low and high pressure levels p_1 and p_2, the working fluid mass flow $\dot{m}$, specific enthalpies h at states 2r and 3 (cf. Fig. 1), the brine outlet temperature, the minimum temperature difference in the ACC, the electical powers on the right-hand side of Eq. (4), and the relative enthalpy drop of the turbine as well as the relative volumetric flow rate at its outlet, see the bottom of Tab. 1.

To describe the remaining thermodynamical quantities of the working fluid in different states (circled labels in Fig. 1), we use existing ANNs, which have been trained and validated in Huster et al. (2019). These ANNs are explicit, analytical representations of individual fluid properties, and thus avoid the need for lookups or iterative computations required when using database-based property models directly. While models incorporating database-based property models typically require black-box optimization, using local or stochastic global approaches, the functional form of the ANN representations allows for their incorporation into deterministic global optimization via our open-source solver MAiNGO.

Some additional functional relationships are expressed via newly generated ANN surrogate models as described in Section 2.1. This allows all model quantities to be explicitly expressed in terms of the variables from Tab. 1 and the ambient temperature. In Sections 2.2–2.4 we give additional detail on the models of the individual components.

Note that the component models are based on a combination of existing modeling approaches from different literature sources. While this allows for the conceptual process design and operation studied in this work, these models should be validated against real plant data before use in a real-world application.

2.1 Explicit Functions from Data via ANNs

Functional relationships between one or more input quantities and an output quantity may be represented as artificial neural networks (ANNs). The benefit of using ANNs as surrogate models within global optimization is twofold:

1. They can be used as explicit alternatives to functional relationships which are otherwise only given implicitly, e.g., in the form of raw data, or via functions containing iterative ele-

Tab. 1. Design and operational variables and their lower and upper bounds. The bounds for the specific enthalpies h_{2r} and h_3 correspond to the saturated liquid at $p = p_{2,\mathrm{LB}}$ and $p = p_{2,\mathrm{UB}}$, respectively.

design variable	**symbol**	**lower bound**	**upper bound**	**unit**
inner shell diameter ECO	$d_{\mathrm{s,ECO}}$	0.7	2.5	m
inner shell diameter EVA	$d_{\mathrm{s,EVA}}$	0.7	2.5	m
inner shell diameter SUP	$d_{\mathrm{s,SUP}}$	0.7	2.5	m
inner shell diameter REC	$d_{\mathrm{s,REC}}$	0.7	2.5	m
relative tube length ECO	$L_{\mathrm{t,ECO}}/d_{\mathrm{s,ECO}}$	4	12	–
relative tube length EVA	$L_{\mathrm{t,EVA}}/d_{\mathrm{s,EVA}}$	4	12	–
relative tube length SUP	$L_{\mathrm{t,SUP}}/d_{\mathrm{s,SUP}}$	4	12	–
relative tube length REC	$L_{\mathrm{t,REC}}/d_{\mathrm{s,REC}}$	4	12	–
relative baffle spacing ECO	$L_{\mathrm{B,ECO}}/d_{\mathrm{s,ECO}}$	0.2	1	–
relative baffle spacing SUP	$L_{\mathrm{B,SUP}}/d_{\mathrm{s,SUP}}$	0.2	1	–
relative baffle spacing REC	$L_{\mathrm{B,REC}}/d_{\mathrm{s,REC}}$	0.2	1	–
ACC heat transfer area	A_{ACC}	1×10^4	1×10^6	m^2
maximum pressure	$p_{\max}$	3	25	bar
nominal fan power	$P_{\mathrm{F,nom}}$	37	200	kW
nominal pump power	$P_{\mathrm{P,nom}}$	0.1	2	MW
nominal turbine power	$P_{\mathrm{T,nom}}$	1	15	MW
design volumetric flow rate	$\dot{V}_{\mathrm{T,o,d}}$	1	50	m^3/s
design specific enthalpy drop	$\Delta h_{\mathrm{T,d}}$	10	65	kJ/kg
Stodola coefficient	K_{S}	0.01	0.05	m^2
operational variable	**symbol**	**LB**	**UB**	**unit**
mass flow rate of isobutane	$\dot{m}$	50	1500	kg/s
low pressure level	p_1	1.1	20	bar
high pressure level	p_2	3	25	bar
specific enthalpy before ECO	h_{2r}	76.105	335.50	kJ/kg
specific enthalpy after ECO	h_3	76.105	335.50	kJ/kg
fan power	P_{F}	0	200	kW
pump power	P_{P}	0.1	2	MW
turbine power	P_{T}	1	15	MW
relative volumetric flow rate	$\dot{V}_{\mathrm{o,rel}}$	0.2	1.2	–
relative specific enthalpy drop	Δh_{rel}	0.2	1.2	–
Brine outlet temperature	$T_{\mathrm{br,o}}$	333.15	403.15	K
ACC minimal temperature difference	$\Delta T_{\mathrm{min,ACC}}$	1	55	K

ments or control structures that cannot be handled by global optimizers directly (e.g., Huster et al., 2019, 2020c).

2. The propagation of tight relaxations for the used activation functions (e.g., tanh) via McCormick relaxations usually results in good relaxations for the overall functional relationship, cf. Schweidtmann and Mitsos (2018). Furthermore, these relaxations are typically much tighter than those of alternative representations for regression models, such as polynomials, see e.g., Schweidtmann et al. (2019). These tighter relaxations generally improve convergence of global optimization.

By varying the number of neurons in each layer and their activation function, different ANN formulations can be generated. The choice of the activation is an active research topic, with common choices being the rectified linear unit (ReLU) and the hyperbolic tangent (tanh). While ReLU networks are inherently nonsmooth, they possess the desirable property of piecewise linearity, and thus can be cast as MILP formulations (see, e.g., Grimstad and Andersson, 2019; Lueg et al., 2021). However, for the present work we preferred the nonlinear but smooth tanh activation, as we already consider several other nonlinearities in our model. All resulting ANN surrogate models used in this work provide sufficient accuracy with a single hidden layer containing up to four neurons. More detailed information on the training is available in the supplementary material.

2.2 Pump

As noted above, the pump only has a minor effect on both P_{net} and TAR. Consequently we use a simple model with constant values for the mechanical efficiency $\eta_{\text{m}} = 0.95$, and the isentropic pump efficiency $\eta_{\text{P}} = 0.80$. With this, the electrical power consumption of the pump is given as:

$$P_{\text{P}} = \dot{m}\,\frac{h_{2,\text{is}} - h_1}{\eta_{\text{m}}\,\eta_{\text{P}}} \tag{6}$$

For the investment costs we use the correlation proposed by Astolfi et al. (2014b), converted from €$_{2014}$ to US$$_{2021}$:

$$C_{\text{I,P}} = 11\,066\,\text{US\$}\,\left(\frac{P_{\text{P,nom}}}{200\,000\,\text{W}}\right)^{0.67} \tag{7}$$

2.3 Turbines

As the overall mass flow rate is split equally between the turbines, we model the electrical power produced by a single turbine as

$$\dot{m}_{\text{T}} = \frac{\dot{m}}{2}, \tag{8}$$

$$P_{\text{T}} = \dot{m}_{\text{T}}\,(h_5 - h_{6,\text{is}})\,\eta_{\text{g}}\,\eta_{\text{T}}, \tag{9}$$

with a generator efficiency of $\eta_{\text{g}} = 0.95$. However, as the turbines are a major contributor to both overall cost and P_{net}, we consider the effect of design (i.e., turbine size) and operation (i.e., part-load) on the turbine efficiency η_{T}, which can be represented as

$$\eta_{\text{T}} = \eta_{\text{T,d}}(\text{SP}, \text{VR}, T_{\text{crit}})\; r\left(\Delta h_{\text{rel}}, \dot{V}_{\text{o,rel}}\right), \tag{10}$$

where the subscript D refers to the design point. Here the maximum achievable isentropic efficiency $\eta_{\text{T,d}}$ is a function of the turbine size parameter SP $= \frac{\dot{V}_{\text{o,is,d}}^{0.5}}{\Delta h_{\text{is,d}}^{0.25}}$, the turbine volume ratio VR $= \frac{\dot{V}_{\text{o,is,d}}}{\dot{V}_{\text{i,d}}}$ and the used working fluid, represented by the respective critical temperature (Macchi and Perdichizzi, 1981; da Lio et al., 2016), and the reduction coefficient r is a function of the relative enthalpy drop Δh_{rel} and the relative volumetric flow $\dot{V}_{\text{o,rel}}$ of the turbine (Ghasemi et al., 2013a; Pili et al., 2019b):

$$\Delta h_{\text{rel}} = \frac{\Delta h}{\Delta h_{\text{d}}} \tag{11}$$

$$\dot{V}_{\text{o,rel}} = \frac{\dot{V}_{\text{o}}}{\dot{V}_{\text{o,d}}} \tag{12}$$

da Lio et al. (2016) computed $\eta_{\text{T,d}}$ for isobutane and several other working fluids. The resulting values show little variation for low values of VR. As in all considered optimizations of the present work VR stayed below 4.25, we assume a fixed value of $\eta_{\text{T,d}} = 0.88$, for simplicity.

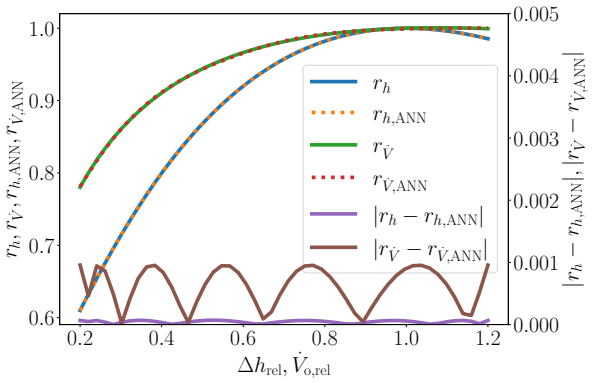

Fig. 2. The two factors r_h and $r_{\dot{V}}$, contributing to efficiency reduction coefficient r from Ghasemi et al. (2013a), their surrogate models $r_{h,\text{ANN}}$ and $r_{\dot{V},\text{ANN}}$, and the resulting errors as a function of the relative enthalpy drop Δh_{rel} and volumetric flow rate $\dot{V}_{\text{o,rel}}$.

Ghasemi et al. (2013a) give a correlation for r[1] that is split into two separate factors, r_h, and $r_{\dot{V}}$, described by polynomials. In order to improve the relaxations of these expressions, we replace the original polynomial form with the following ANN surrogate models:

$$\begin{aligned} r_h &= 0.21395 \\ &\quad + 0.77056\,\tanh(0.064155 + 1.7140\,\Delta h_{\text{rel}}) \\ &\quad + 0.10029\,\tanh(2.8276 - 2.1628\,\Delta h_{\text{rel}}) \end{aligned} \tag{13}$$

$$\begin{aligned} r_{\dot{V}} &= 0.70472 \\ &\quad - 0.27582\,\tanh(0.39630 - 3.7982\,\dot{V}_{\text{o,rel}}) \\ &\quad - 0.020017\,\tanh(3.1786 - 5.0984\,\dot{V}_{\text{o,rel}}) \end{aligned} \tag{14}$$

The comparison with the original correlation and the absolute error can be seen in Fig. 2.

Another important performance aspect is the relationship between reduced mass flow rate ϕ, defined as

$$\phi = \frac{\dot{m}_{\text{T}}}{\sqrt{\rho_5\,p_5}}, \tag{15}$$

and pressure ratio

$$\text{PR} = \frac{p_6}{p_5} = \frac{p_1}{p_2}. \tag{16}$$

For classical Rankine cycles, Stodola's ellipse law is commonly used to describe this relationship. Despite the fact that this correlation is only valid

[1] Note that the journal publication is missing a 0 in one of the coefficients, the correct correlation can be found in the preprint (Ghasemi et al., 2013b).

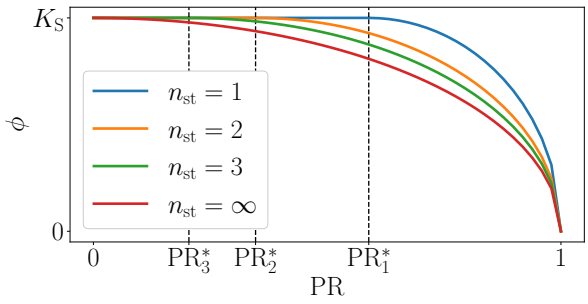

Fig. 3. Comparison of Stodola's ellipse law ($n_{st} = \infty$), presenting reduced mass flow rate ϕ, limited by the Stodola coefficient (K_S), as a function of pressure ratio (PR), and Cooke's adaption (Cooke, 1984) for finite stage number (n_{st}) and possibly choked conditions (*) for the working fluid isobutane ($\kappa = 1.08$).

for an infinite number of unchoked stages (Cooke, 1984), it is frequently used for modeling ORC turbines, see, e.g., Calise et al. (2014); Capra and Martelli (2015); Mazzi et al. (2015); Pili et al. (2017), even though ORC turbines commonly have between one and three stages (Macchi and Astolfi, 2017b).

As cycles operating with isobutane allow for high efficiencies at low volume ratios (see, e.g., da Lio et al., 2016), a reasonable initial assumption for the number of stages n_{st} is 1, as this keeps the turbine compact and thus cheap (Macchi and Astolfi, 2017a). We therefore assume a single stage turbine and use a generalization of Stodola's ellipse law proposed by Cooke (1984). Cooke's generalization accounts for choking if PR sinks below the value corresponding to an isentropic expansion to sonic conditions PR^*, also see Fig. 3,

$$PR^* = \left(\frac{2}{\kappa+1}\right)^{\frac{n_{st}\,\kappa}{\kappa-1}}, \tag{17}$$

$$K_S = \frac{\phi}{\sqrt{1-\left(\frac{\max(0,\,PR-PR^*)}{1-PR^*}\right)^2}}, \tag{18}$$

where we use a fixed isentropic expansion coefficient for isobutane of $\kappa = 1.08$, n_{st} is the number of turbine stages, and K_S is the Stodola coefficient, a design variable proportional to the flow cross-section of the turbine.

For the cost of turbine and generator, we use a correlation from Astolfi et al. (2014b) that takes into account both the number of stages n_{st}, and the turbine size parameter SP for the costs of the turbine, as well as the turbine power P_T, for the costs of the electrical generator. Again costs have been converted from €$_{2014}$ to US$$_{2021}$:

$$C_{I,T} = 972\,241\,\text{US\$}\left(\frac{n_{st}}{2}\right)^{0.5}\left(\frac{SP}{0.18\,\text{m}}\right)^{1.1} + 15\,809\,\text{US\$}\left(\frac{P_{T,nom}}{5\,\text{MW}}\right)^{0.67} \tag{19}$$

Note that the problems solved in this work assume a fixed stage number of $n_{st} = 1$ for simplicity, however, the presented model can also handle higher numbers, or even the introduction of n_{st} as a design variable.

2.4 Heat Exchangers

We assume that the economizer (ECO), superheater (SUP), and recuperator (REC) are fixed tube sheet shell & tube exchangers, while the evaporator (EVA) is a shell and tube reboiler, and that heat is rejected via an air-cooled condenser (ACC).

It is common practice to model total heat transfer coefficients U_{HX} in off-design conditions as

$$U_{HX} = U_{HX,d}\left(\frac{\dot{m}}{\dot{m}_d}\right)^{F_{U,HX}}, \tag{20}$$

where $F_{U,HX}$ is a constant, obtained from simulations or measurements (see e.g., Capra and Martelli, 2015; Pili et al., 2019a). However, apart from $\dot{m}$, U_{HX} generally also depends on pressures, temperatures, and heat exchanger geometry, which is not reflected in Eq. (20). Instead of Eq. (20), we therefore use empirical correlations for the total heat transfer coefficients U_{HX}, which explicitly account for heat exchanger geometries. The heat transfer area A_{HX} is correlated with thermal quantities via

$$A_{HX} = \dot{Q}_{HX}\,U_{HX}^{-1}\Delta T_{ln,HX}^{-1}F_{T,HX}^{-1}. \tag{21}$$

Here $\dot{Q}_{HX}$ is the exchanged heat, $\Delta T_{ln,HX}$ the logarithmic mean temperature difference, and $F_{T,HX}$ a correction factor for a particular heat exchanger HX. For U_{HX}, the denominators of Eqs. (47), (73) and (78) are used for the respective inverse terms in Eq. (21). Further details on the component-specific correlations for U_{HX} and A_{HX} can be found in Sections 2.4.1 and 2.4.2. In the following, we drop the subscript HX whenever it is not necessary for clarity.

The inverse of the logarithmic mean temperature difference is a convex function of $T_{h,i} - T_{c,o}$ and $T_{h,o} - T_{c,i}$, and takes the form

$$\Delta T_{ln}^{-1} = \frac{\ln\left(\frac{T_{h,i}-T_{c,o}}{T_{h,o}-T_{c,i}}\right)}{(T_{h,i}-T_{c,o})-(T_{h,o}-T_{c,i})}, \tag{22}$$

where the subscripts h and c refer to the hot and cold fluid, and i and o to the inlet and outlet, respectively. Instead of directly using the right-hand side of Eq. (22) in Eq. (21), we use an internal function, implementing $\Delta T_{\ln}^{-1}$ and making its convexity visible to the optimizer, resulting in better relaxations (cf. Mistry and Misener, 2016; Najman and Mitsos, 2016). The logarithmic mean temperature difference is valid for pure cross-flow or for the case where one fluid is isothermal, i.e., for evaporation or condensation. For other situations a temperature correction factor $F_T \leq 1$ is used to adjust the temperature difference, see, e.g., Kuppan (2013); Serth (2007).

The cost for the heat exchangers is calculated via the established cost correlations from Turton et al. (2018), adjusted to US$$_{2021}$$ via the Chemical Engineering Plant Cost Index (CEPCI):

$$C_{\mathrm{I,HX},0} = \mathrm{cf}(A_{\mathrm{o,HX}}, F_{\mathrm{HX},1}, F_{\mathrm{HX},2}, F_{\mathrm{HX},3}) \tag{23}$$

$$F_{\mathrm{HX},0} = F_{\mathrm{HX},4} + F_{\mathrm{HX},5}\, F_{\mathrm{HX,mat}}\, F_{\mathrm{HX},p} \tag{24}$$

$$C_{\mathrm{I,HX}} = \frac{\mathrm{CEPCI}_{2021}}{\mathrm{CEPCI}_{2001}} C_{\mathrm{I,HX},0}\, F_{\mathrm{HX},0}, \tag{25}$$

where cf is the Guthrie cost function

$$\mathrm{cf}(x,a,b,c) = 10^{a+b\,\log_{10}(x)+c\,\log_{10}(x)^2}, \tag{26}$$

and the pressure correction factor is calculated as

$$\hat{p}_{\mathrm{HX}} = p_{\max} - 1\,\mathrm{bar} \tag{27}$$

$$F_{\mathrm{HX},p} = \mathrm{cf}(\hat{p}_{\mathrm{HX}}, 0.03881, -0.11272, 0.08183), \tag{28}$$

except for $F_{\mathrm{ACC},p}$ which is 1. The values of the numerical coefficients $F_{\mathrm{HX},i}$, $i \in \{1, \cdots, 5\}$, and $F_{\mathrm{HX,mat}}$ are given in Tab. 2. For the shell & tube exchangers, the overall outer tube area $A_{\mathrm{o,HX}}$ corresponds to the total heat exchange area A_{HX}, while for the ACC, the latter is larger due to the use of finned tubing, also see Section 2.4.2. The velocities of all fluids flowing within the tubes and the shells are limited to $v_{\max} = 3\,\frac{\mathrm{m}}{\mathrm{s}}$ for liquids and to $v_{\max} = 20\,\frac{\mathrm{m}}{\mathrm{s}}$ for gases.

2.4.1 Shell & Tube Heat Exchangers

For the shell and tube type exchangers, we assume triangular tube arrangement and fixed values for the tube pitch L_{p}, outer and inner tube diameter d_{o} and d_{i} according to Ghasemi et al. (2013a), while the tube length L_{t} and baffle spacing L_{B} are expressed via variable ratios with respect to the inner shell diameter d_{s}, c.f. Tab. 1. The number of tube passes n_{tp} is assumed to be 2 for the evaporator and 1 for all other exchangers, resulting in $F_T = 1$

Tab. 2. Coefficients for heat exchanger cost correlations, taken from Turton et al. (2018). For ECO, SUP, and REC, we take the coefficients for fixed-tubesheet exchangers, and for EVA those for U-tube exchangers. Note that the coefficients for the kettle-reboilers which might be considered as an alternative for EVA are only valid for small units up to $100\,\mathrm{m}^2$. We assume all shell & tube exchangers are manufactured from stainless steel and the ACC from carbon steel.

	ECO, SUP, REC	EVA	ACC
$F_{\mathrm{HX},1}$	4.3247	4.4646	4.0336
$F_{\mathrm{HX},2}$	−0.3030	−0.5277	0.2341
$F_{\mathrm{HX},3}$	0.1634	0.3955	0.0497
$F_{\mathrm{HX},4}$	1.63	1.63	0.96
$F_{\mathrm{HX},5}$	1.66	1.66	1.21
$F_{\mathrm{HX,mat}}$	2.75	2.75	1

Tab. 3. Geometry for shell and tube type exchangers. The values for n_{tp} were assumed, the remaining values are taken from Ghasemi et al. (2013a).

HX	n_{tp}	L_{p} [mm]	d_{o} [mm]	d_{i} [mm]
EVA	2	20.64	15.88	14.23
ECO	1	20.64	15.88	14.23
SUP	1	20.64	15.88	14.23
REC	1	39.69	31.75	29.64

in all cases . The resulting geometry is summarized in Tab. 3.

With the assumed parameters, the tube bundle diameter d_{tb}, tube number n_{t} and heat exchanger area A_{o} can be obtained as discussed by Kuppan (2013):

$$d_{\mathrm{tb}} = d_{\mathrm{s}} - \left(0.005\,\mathrm{m} + \frac{0.012\,\mathrm{m}}{d_{\mathrm{s}}}\right) \tag{29}$$

$$n_{\mathrm{t}} = \frac{1.56}{\sqrt{3}} \left(\frac{d_{\mathrm{tb}} - d_{\mathrm{o}}}{L_{\mathrm{p}}}\right)^2 \tag{30}$$

$$A_{\mathrm{o}} = \pi\, d_{\mathrm{o}} L_{\mathrm{t}} n_{\mathrm{t}} \tag{31}$$

Additionally, we consider the cross-sectional areas available for tube- and shell-side flow (index t and s, respectively):

$$A_{\mathrm{t,cs}} = \pi \frac{d_{\mathrm{i}}^2}{4} \frac{n_{\mathrm{t}}}{n_{\mathrm{tp}}} \tag{32}$$

$$A_{\mathrm{s,cs}} = L_{\mathrm{B}} \left(d_{\mathrm{s}} - d_{\mathrm{tb}} + (d_{\mathrm{tb}} - d_{\mathrm{o}}) \left(1 - \frac{d_{\mathrm{o}}}{L_{\mathrm{p}}}\right)\right) \tag{33}$$

Using these cross-sectional areas, we can express limits on the flow velocities

$$\dot{V}_{\mathrm{t,max}} \leq A_{\mathrm{t,cs}}\, v_{\mathrm{max}}, \tag{34}$$

$$\dot{V}_{\mathrm{s,max}} \leq A_{\mathrm{s,cs}}\, v_{\mathrm{max}}, \tag{35}$$

where v_{max} is set to the limit for liquids or gases, depending on the phase of the respective fluid.

Exchangers with Single Phase Fluids

In the economizer, superheater and recuperater both hot and cold fluids are all single phase shell and tube exchangers. For the hot fluid (subscript h), which flows on the tube-side, the Gnielinski correlation (Gnielinski, 1976, 1983) is used:

$$\mathrm{Re_t} = \frac{4\,\dot{m}_{\mathrm{h}}\, n_{\mathrm{tp}}}{\pi\, d_{\mathrm{i}}\, n_{\mathrm{t}}\, \overline{\mu}_{\mathrm{h}}} \tag{36}$$

$$F_{\mathrm{D}} = (0.782\,\ln(\mathrm{Re_t}) - 1.51)^{-2} \tag{37}$$

$$F_{\mathrm{e}} = 1 + \left(\frac{d_{\mathrm{i}}}{L_{\mathrm{t}}}\right)^{2/3} \tag{38}$$

$$\mathrm{Nu_t} = \frac{F_{\mathrm{D}}/8\,(\mathrm{Re_t} - 1000)\overline{\mathrm{Pr}}_{\mathrm{h}}}{1 + 12.7\sqrt{F_{\mathrm{D}}/8}\left(\overline{\mathrm{Pr}}_{\mathrm{h}}^{2/3} - 1\right)} F_{\mathrm{e}} \tag{39}$$

$$\alpha_{\mathrm{t}} = \mathrm{Nu_t}\frac{\overline{k}_{\mathrm{h}}}{d_{\mathrm{i}}} \tag{40}$$

Here F_{D} is the Darcy friction factor and F_{e} a correction for entry effects. The fluid properties $\overline{\mu}_{\mathrm{h}}$, $\overline{\mathrm{Pr}}_{\mathrm{h}}$, and $\overline{k}_{\mathrm{h}}$ are evaluated at $(T, p) = (\overline{T}_{\mathrm{h}}, p_{\mathrm{h}})$.

For the cold fluid (subscript c) flowing on the shell-side, we use the simplified Delaware method as described by Kern and Kraus (1972) (also see Serth (2007)), to describe the heat transfer coefficient:

$$d_{\mathrm{eq}} = \frac{2\sqrt{3}\,L_{\mathrm{p}}^2}{\pi d_{\mathrm{o}}} - d_{\mathrm{o}} \tag{41}$$

$$\mathrm{Re_s} = \frac{d_{\mathrm{eq}}\,\dot{m}_{\mathrm{c}}}{A_{\mathrm{s,cs}}\,\overline{\mu}_{\mathrm{c}}} \tag{42}$$

$$F_{\mathrm{C}} = \frac{1 + \frac{L_{\mathrm{B}}}{d_{\mathrm{s}}}}{2}\left(0.08\,\mathrm{Re}_s^{0.6821} + 0.7\,\mathrm{Re}_s^{0.1772}\right) \tag{43}$$

$$\mathrm{Nu_s} = F_{\mathrm{C}}\,\overline{\mathrm{Pr}}_{\mathrm{c}}^{1/3}\left(\frac{\overline{\mu}_{\mathrm{c}}}{\mu_{\mathrm{c}}(\overline{T}_{\mathrm{w}}, p_{\mathrm{c}})}\right)^{0.14} \tag{44}$$

$$\alpha_{\mathrm{s}} = \mathrm{Nu_s}\frac{\overline{k}_{\mathrm{c}}}{d_{\mathrm{eq}}} \tag{45}$$

Here F_{C} is the Colburn factor and the fluid properties $\overline{\mu}_{\mathrm{c}}$, $\overline{\mathrm{Pr}}_{\mathrm{c}}$, and $\overline{k}_{\mathrm{c}}$ are evaluated at $(T, p) = (\overline{T}_{\mathrm{c}}, p_{\mathrm{c}})$ and

$$\overline{T}_{\mathrm{w}} = \frac{\overline{T}_{\mathrm{c}} + \overline{T}_{\mathrm{h}}}{2}. \tag{46}$$

The overall heat transfer coefficient is then given by

$$U_{\mathrm{S\&T}}^{-1} = \frac{d_{\mathrm{o}}}{d_{\mathrm{i}}}\frac{1}{\alpha_{\mathrm{t}}} + d_{\mathrm{o}}\frac{\ln(d_{\mathrm{o}}/d_{\mathrm{i}})}{2\,k_{\mathrm{t}}} + \frac{1}{\alpha_{\mathrm{s}}} + F_{\mathrm{R}}, \tag{47}$$

where we use $k_{\mathrm{t}} = 16\,\frac{\mathrm{W}}{\mathrm{m\,K}}$ as the thermal conductivity of the tube material (stainless steel, Serth (2007)), and a factor for fouling resistance of $F_{\mathrm{R}} = 1.3 \times 10^4\,\frac{\mathrm{m^2\,K}}{\mathrm{W}}$ (Hernandez-Galan and Plauchu, 1989).

Evaporator

For the tube side heat transfer coefficient, we again use Eqs. (36)–(40) while for the shell side, where the isobutane is boiled on horizontal tubes, we follow the approach proposed in Serth (2007) and correct a coefficient for nucleate boiling (subsctipt nb) to account for convective effects. The resulting heat transfer coefficient for boiling (subscript b) can then be obtained through the following correlations:

$$p_{\mathrm{c,rel}} = \frac{p_{\mathrm{c}}}{p_{\mathrm{c,crit}}} \tag{48}$$

$$\Delta T_{\mathrm{w}} = \overline{T}_{\mathrm{w}} - T_{\mathrm{sat}} \tag{49}$$

$$F_p = 1.8\,p_{\mathrm{c,rel}}^{0.17} + 4\,p_{\mathrm{c,rel}}^{1.2} + 10\,p_{\mathrm{c,rel}}^{10} \tag{50}$$

$$\alpha_{\mathrm{nb}} = 1.4692 \times 10^{-15}\,p_{\mathrm{c,crit}}^{2.3}\,\Delta T_{\mathrm{w}}^{7/3}\,F_p^{10/3} \tag{51}$$

$$F_{\mathrm{b}} = 1 + 0.1\left(0.90644\,\frac{d_{\mathrm{tb}}\,d_{\mathrm{o}}}{L_{\mathrm{p}}^2} - 1\right)^{0.75} \tag{52}$$

$$\alpha_{\mathrm{b}} = \alpha_{\mathrm{nb}}\,F_{\mathrm{b}} + 250 \tag{53}$$

Eq. (51) is the Mostinski correlation for nucleate boiling, adjusted to SI units.

The overall heat transfer coefficient is again calculated via Eq. (47) with α_{b} instead of α_{s}. Following Serth (2007), we use the saturation temperature for all calculations related to ΔT_{ln} and F_T, instead of the inlet temperature of the potentially subcooled liquid. Note that by fixing the geometry, the working fluid at the evaporator inlet will not necessarily be saturated when considering multiple operating points, but instead is determined by Eq. (21). We therefore introduce the enthalpy of the working fluid at the outlet of the economizer as an auxiliary variable, and limit its value to lie between 95%–100% of the saturated value at the given pressure.

2.4.2 Air-Cooled Condenser (ACC)

For the ACC, we assume horizontal bundles of finned tubes, arranged in multiple rows, again following Ghasemi et al. (2013a), but allowing for different heat exchanger areas via a variable number of tubes n_{t}. The resulting values for tube and fin

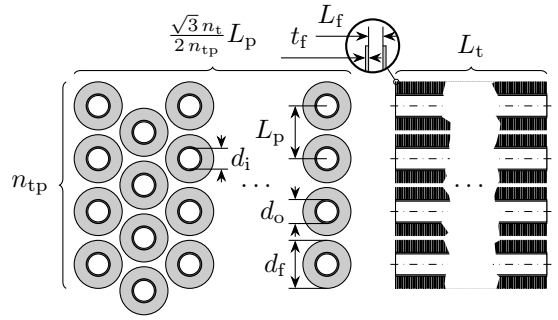

Fig. 4. Assumed geometry for the ACC: Number of tubes n_t, tube passes n_{tp}, tube length L_t, tube pitch L_p, diameters of inner tube d_i, outer tube d_o, and fin d_f, fin thickness t_f, and spacing L_f. Left: cross-section, right: side view. Note that each tube pass corresponds to a single tube row.

dimensions and spacing are given in Tab. 4, for the assumed geometry, see Fig. 4.

The tube number n_t can then be expressed as a linear function of the overall heat transfer area A_{ACC}, i.e.,

$$\begin{aligned} n_t &= \frac{A_{ACC}}{L_t\,\pi\left[d_o + \frac{\frac{d_f^2-d_o^2}{2}+t_f\,(d_f-d_o)}{L_f+t_f}\right]} \\ &= 0.050307\,A_{ACC}, \end{aligned} \tag{54}$$

where d_f is the fin diameter, t_f the fin thickness and L_f the fin spacing, also see Fig. 4. Note that since n_t is in the order of 1000 – 10 000, the effect of its integrality is negligible.

For the air-side heat transfer coefficient we first calculate the Reynolds number based on the maximum air velocity as given in Serth (2007):

$$A_{face} = \frac{\sqrt{3}\,n_t}{2\,n_{tp}}\,L_p L_t \tag{55}$$

$$v_{face} = \frac{\dot{m}_{air}}{\rho_{air}(T_{air,i})\,A_{face}} \tag{56}$$

$$v_{air,max} = \frac{v_{face}\,L_p\,(L_f+t_f)}{L_p - d_o - (d_f-d_o)\,t_f} \tag{57}$$

$$\mathrm{Re}_{air} = \frac{d_o\,v_{air,max}\,\overline{\rho}_{air}}{\overline{\mu}_{air}} \tag{58}$$

For the calculation of the heat transfer coefficient, we use the correlation of Ganguli et al. (1985):

$$A_{o,rel} = \frac{A_o}{A_{ACC}} \tag{59}$$

$$\mathrm{Nu}_{air} = 0.38\,\mathrm{Re}_{air}^{0.6}\,\overline{\mathrm{Pr}}_{air}^{1/3}\,A_{o,rel}^{0.15} \tag{60}$$

$$\alpha_{air} = \mathrm{Nu}_{air}\frac{\overline{k}_{air}}{d_o} \tag{61}$$

Here A_{ACC} is the total area that is in contact with air, including the fin surface, and $\overline{\rho}_{air}, \overline{\mu}_{air}, \overline{\mathrm{Pr}}_{air}$, and $\overline{k}_{air}$ are evaluated at $(T,p) = (\overline{T}_{air}, 1\,\mathrm{atm})$.

The desuperheating (DES) and condensation (CON) sections need to be considered separately, as these regions may exhibit very different heat transfer coefficients and temperature differences.

While in the condensing section the isobutane is isothermal, and hence, $F_{T,CON} = 1$, $F_{T,DES}$ needs to be determined via an appropriate correlation. In preliminary calculations with various ambient temperatures, desuperheating occured mostly within the first tube-row of the ACC. We therefore determine $F_{T,DES}$ based on the correlation of Schedwill (1968) for a single row of finned tubes, also see Kuppan (2013):

$$e_h = \frac{T_{6r} - T_{pinch}}{T_{6r} - T_{air,pinch}} \tag{62}$$

$$e_c = \frac{T_{air,o} - T_{air,pinch}}{T_{6r} - T_{air,pinch}} \tag{63}$$

$$F_{T,DES} = \frac{e_c\,\ln\left(\frac{1-e_h}{1-e_c}\right)}{(e_h - e_c)\,\ln\left(\frac{e_c}{e_h}\,\ln(1-e_h)+1\right)} \tag{64}$$

Here e_h and e_c are the effectiveness of the hot and the cold stream, i.e., isobutane and air, respectively. The temperatures T_{pinch} and $T_{air,pinch}$ refer to the isobutane and air temperatures at the point of minimal temperature difference, i.e., the beginning of condensation. Note that Eq. (64) is indeterminate for $e_h = e_c$ as well as for

$$e_c \geq e_{c,lim} = -\frac{e_h}{\ln(1-e_h)}, \tag{65}$$

also see Fig. 5. These two facts complicate the use of Eq. (64) in global optimization. We thus generate an ANN representing the inverse of $F_{T,DES}$, needed in Eq. (21). As pointed out by Ahmad et al. (1988) and Smith (2005), both low values of F_T, as well as regions where F_T has a steep slope should be avoided, as they correspond to an excessive temperature cross and the risk for larger errors in the predicted heat transfer, respectively. To achieve this, we scale the limit in Eq. (65) by 90% and consider

Tab. 4. Assumed tube and fin geometry for air cooled condenser. The number of tube passes and tube length ($\hat{=}\,36\,\mathrm{ft}$) are typical values (Serth, 2007), the remaning values are taken from Ghasemi et al. (2013a).

n_{tp} [–]	L_{t} [m]	L_{p} [mm]	d_{f} [mm]	d_{o} [mm]	d_{i} [mm]	L_{f} [mm]	t_{f} [mm]
4	10.97	69.85	63.5	31.75	27.53	1.9	0.41

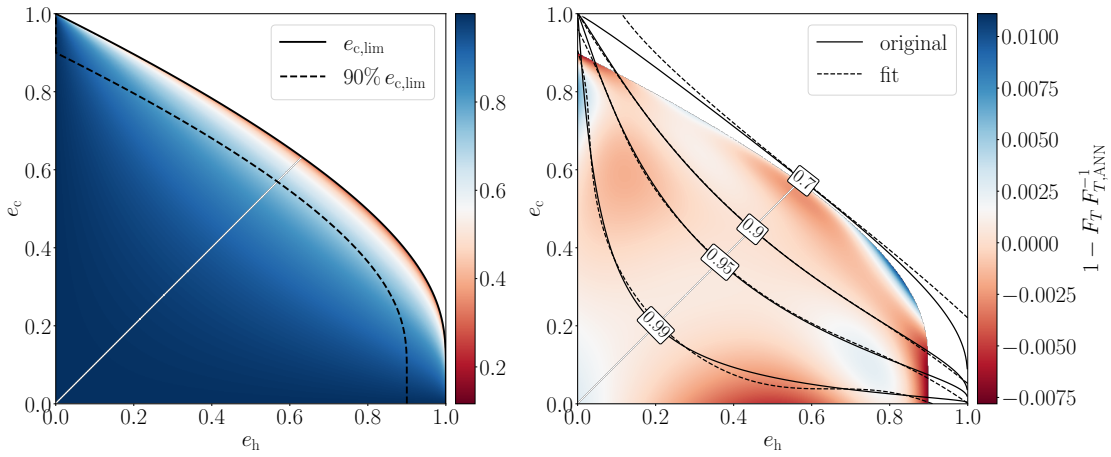

Fig. 5. Left: Schedwill correlation for F_T for cross-flow over a finned tube (Eq. (64)). Note that the function is indeterminate for $e_{\mathrm{h}} = e_{\mathrm{c}}$ as well as for $e_{\mathrm{c}} \geq e_{\mathrm{c,lim}}$ (Eq. (65)). Right: Error for the resulting ANN representing inverse F_T and contours for F_T based on the original correlation and the fit.

only data that satisfies

$$e_{\mathrm{c}} \leq -\frac{e_{\mathrm{h}}}{\ln(1 - e_{\mathrm{h}}/0.9)}. \tag{66}$$

The resulting ANN surrogate model takes the form

$$\begin{aligned} F_{T,\mathrm{ANN}}^{-1}(e_{\mathrm{h}}, e_{\mathrm{c}}) = {} & 0.60127 \\ & - 1.9843 \tanh(3.1595 - 2.3103\, e_{\mathrm{h}} - 1.6979\, e_{\mathrm{c}}) \\ & + 1.9843 \tanh(3.8096 + 2.0196\, e_{\mathrm{h}} - 2.3837\, e_{\mathrm{c}}) \\ & - 0.22447 \tanh(9.6024 - 6.5102\, e_{\mathrm{h}} - 9.3455\, e_{\mathrm{c}}) \\ & + 0.61916 \tanh(2.8588 - 2.7623\, e_{\mathrm{h}} - 1.2156\, e_{\mathrm{c}}) \end{aligned} \tag{67}$$

and has its largest error of about 1% close to the boundary of the domain, also see Fig. 5.

For the desuperheating section, α_{t} is calculated using Eqs. (36), (37), (39) and (40) and $F_{\mathrm{E}} = 1$ since $d_{\mathrm{i}} \ll L_{\mathrm{t}}$. Neglecting fouling and the contact resistance between fins and tubing, the overall coefficient based on A_{ACC} can then be computed as described in Serth (2007):

$$F_{\mathrm{f}} = \frac{d_{\mathrm{f}} + t_{\mathrm{f}} - d_{\mathrm{o}}}{2}\left[1 + 0.35\,\ln\left(\frac{d_{\mathrm{f}} + t_{\mathrm{f}}}{d_{\mathrm{o}}}\right)\right] \tag{68}$$

$$F_{\alpha} = \sqrt{\frac{2\,\alpha_{\mathrm{air}}}{k_{\mathrm{f}}\, t_{\mathrm{f}}}} \tag{69}$$

$$\eta_{\mathrm{f}} = \frac{\tanh(F_{\mathrm{f}}\, F_{\alpha})}{F_{\mathrm{f}}\, F_{\alpha}} \tag{70}$$

$$\eta_{\mathrm{wf}} = \frac{A_{\mathrm{o,air}} + \eta_{\mathrm{f}}\, A_{\mathrm{f}}}{A_{\mathrm{ACC}}} \tag{71}$$

$$A_{\mathrm{i,rel}} = \frac{A_{\mathrm{i}}}{A_{\mathrm{ACC}}} \tag{72}$$

$$U_{\mathrm{DES}}^{-1} = \frac{1}{\alpha_{\mathrm{t}}\, A_{\mathrm{i,rel}}} + \frac{A_{\mathrm{ACC}}}{\pi\, L_{\mathrm{t}}}\,\frac{\ln\left(d_{\mathrm{o}}/d_{\mathrm{i}}\right)}{2\, k_{\mathrm{t}}} + \frac{1}{\alpha_{\mathrm{air}}\, \eta_{\mathrm{wf}}} \tag{73}$$

Here $A_{\mathrm{o,air}}$ is the outer tube area that is in direct contact with air, i.e., excluding area in contact with fins, A_{f} is the total fin area, $k_{\mathrm{f}} = 237\,\frac{\mathrm{W}}{\mathrm{mK}}$ is the thermal conductivity of the aluminum fins and η_{wf} is the weighted fin efficiency.

In the condensation section, the local heat transfer coefficient within the tubes can be described by Shah's correlation (Shah, 1979, 2009):

$$F_x = (1-x)^{0.8} + \frac{3.8\,x^{0.76}(1-x)^{0.04}}{p_{\mathrm{h,rel}}^{0.38}} \tag{74}$$

$$\alpha_{\mathrm{con}}(x) = 0.023\,\mathrm{Re}_{\mathrm{sat}}^{0.8}\,\mathrm{Pr}_{\mathrm{h,sat}}^{0.4}\,\frac{k_{\mathrm{h,sat}}}{d_{\mathrm{i}}}\,F_x, \tag{75}$$

where x is the vapor quality. Here $\mathrm{Re}_{\mathrm{sat}}$ is calculated as in Eq. (36) with $\overline{\mu}_{\mathrm{h}}$ replaced by $\mu_{\mathrm{h}}(T_{\mathrm{h,sat}}, p_{\mathrm{h}})$, and similarly $\mathrm{Pr}_{\mathrm{h,sat}}$ and $k_{\mathrm{h,sat}}$ are evaluated at $(T,p) = (T_{\mathrm{h,sat}}, p_{\mathrm{h}})$. As proposed by Shah, we assume a linear variation of the vapor quality and integrate Eq. (74) to obtain an average heat transfer coefficient that may be used for the complete condensation:

$$\overline{F}_x = 5/9 + \frac{2.0434}{p_{\mathrm{h,rel}}^{0.38}} \tag{76}$$

$$\overline{\alpha}_{\mathrm{con}} = 0.023\,\mathrm{Re}_{\mathrm{sat}}^{0.8}\,\mathrm{Pr}_{\mathrm{h,sat}}^{0.4}\,\frac{k_{\mathrm{h,sat}}}{d_{\mathrm{i}}}\,\overline{F}_x \tag{77}$$

As in the desuperheating section the overall heat transfer coefficient can be computed as:

$$U_{\mathrm{CON}}^{-1} = \frac{1}{\overline{\alpha}_{\mathrm{con}}\,A_{\mathrm{i,rel}}} + \frac{A_{\mathrm{ACC}}}{\pi\,L_{\mathrm{t}}}\,\frac{\ln(d_{\mathrm{o}}/d_{\mathrm{i}})}{2\,k_{\mathrm{t}}} + \frac{1}{\alpha_{\mathrm{air}}\,\eta_{\mathrm{wf}}} \tag{78}$$

With the respective quantities for the desuperheating and condensing sections, the overall area of the ACC must satisfy

$$\begin{aligned} A_{\mathrm{ACC}} &= A_{\mathrm{DES}} + A_{\mathrm{CON}} \\ &= \left(\dot{Q}U^{-1}\,\Delta T_{\ln}^{-1}\,F_T^{-1}\right)_{\mathrm{DES}} \\ &\quad + \left(\dot{Q}U^{-1}\,\Delta T_{\ln}^{-1}\right)_{\mathrm{CON}}. \end{aligned} \tag{79}$$

Note that for the condensation section F_T is equal to 1 due to the isothermal phase change.

The electrical power for each fan is calculated as

$$P_{\mathrm{F}} = \frac{\Delta p_{\mathrm{F}}\dot{V}_{\mathrm{air}}}{n_{\mathrm{F}}\,\eta_{\mathrm{F}}}, \tag{80}$$

where n_{F} is the total number of fans and an overall efficiency of $\eta_{\mathrm{F}} = 0.7$ is assumed. The necessary pressure difference Δp_{F}, provided by the fan is derived from the air-side pressure drop based on correlations from Ganguli et al. (1985):

$$\mathrm{Re}_{\mathrm{eff}} = \mathrm{Re}_{\mathrm{air}}\,\frac{2\,L_{\mathrm{f}}}{d_{\mathrm{f}} - d_{\mathrm{o}}} \tag{81}$$

$$F_{\mathrm{air}} = \frac{L_{\mathrm{p}} - d_{\mathrm{f}}}{d_{\mathrm{o}}} \tag{82}$$

$$F_{\mathrm{Re}} = \frac{1 + 2\,\frac{\exp(-F_{\mathrm{air}}/4)}{1+F_{\mathrm{air}}}}{0.021 + \frac{27.2}{\mathrm{Re}_{\mathrm{eff}}} + \frac{0.29}{\mathrm{Re}_{\mathrm{eff}}^{0.2}}} \tag{83}$$

$$\Delta p_{\mathrm{air}} = 2\,F_{\mathrm{Re}}\,n_{\mathrm{tp}}\,\rho_{\mathrm{air}}\,v_{\mathrm{air,max}}^2 \tag{84}$$

$$\Delta p_{\mathrm{F}} = 1.2\,\Delta p_{\mathrm{air}} \tag{85}$$

In Eq. (85) we follow the assumption from Serth (2007) and account for 20% of additional losses caused by the support structure, screens, etc.

The number of fans is determined from the total width of the ACC, see Fig. 4. Dividing this width by two gives the width of each of the banks, and as the fan bays are approximately square, dividing by L_{t} and flooring yields the number of bays per bank. Doubling this value gives the total number of bays which by assumption is equal to the number of fans n_{F}, i.e.:

$$W_{\mathrm{tot}} = \frac{\sqrt{3}\,n_{\mathrm{t}}}{2\,n_{\mathrm{tp}}}L_{\mathrm{p}} \tag{86}$$

$$n_{\mathrm{F}} = 2\left\lfloor \frac{W_{\mathrm{tot}}}{2\,L_{\mathrm{t}}} \right\rfloor \tag{87}$$

Fan costs are modeled as in Smith (2005), with costs adjusted from US$$_{2000}$$ to US$$_{2021}$$:

$$C_{\mathrm{I,F}} = 18\,991\,\mathrm{US\$}\,n_{\mathrm{F}}\left(\frac{P_{\mathrm{F,nom}}}{50\,\mathrm{kW}}\right)^{0.76} \tag{88}$$

3 Computational Results

We implemented the component models presented in Section 2 and aggregated them to a system model representing the considered ORC, using our open-source modeling framework COMANDO (Langiu et al., 2021). The source code is available under `examples\ORC_off-design` in the COMANDO repository. Based on this system model, we define multiple optimization problems considering TAR as the objective with operational scenarios characterized by different ambient temperatures, i.e., $\xi = T_{\mathrm{amb}}$. As in Ghasemi et al. (2013a), we consider the ORC system to be built at a location exhibiting an ambient temperature distribution as shown in Fig. 6, with a weighted average temperature of $\overline{T}_{\mathrm{amb}} = 15.85\,^{\circ}\mathrm{C}$ (289 K). The different problems we consider are solved using our open-source deterministic global optimization solver MAiNGO

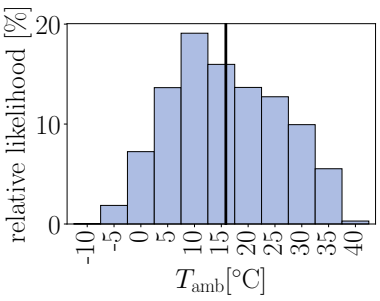

Fig. 6. Assumed distribution of daily ambient temperatures considered for the case study, adjusted from Ghasemi et al. (2013a). The vertical line depicts the weighted average of $\overline{T}_{amb} = 15.85\,°C$.

(Bongartz et al., 2018) on an Intel i7-8700 CPU (3.20 GHz) with 32 GB of RAM. Solutions to these problems consist of optimal design decisions and one set of optimal operational decisions for each considered value of T_{amb}, according to Tab. 1.

In all performed optimizations, only a single local solution is found during preprocessing. Note that due to the nonconvexity, the problems may in principle have multiple local solutions. Given the large number of variables ($19 + 12 \times |\Xi|$), it is not possible to perform a dense search of the entire feasible space during preprocessing, and the ten randomly generated initial points might all converge to the same local minimum. To obtain a global solution, MAiNGO employs branch and bound, however, the level of detail considered in the system model results in a large formulation ($4 + 81 \times |\Xi|$ inequality, and $11 \times |\Xi|$ equality constraints) and as a consequence, in high computational cost. In particular, the upper bounds decrease very slowly for the considered optimizations, and the local solution from preprocessing is never improved, even for computation times up to one day.

Note that we use a reduced-space formulation, i.e., we directly use expressions describing intermediate quantities within other expressions instead of introducing optimization variables for them. A typical full-space formulation would introduce variables and add corresponding equality constraints for temperatures and enthalpies in all states, as well as for several other intermediate quantities, required for the calculation of component behavior. For the present problem this would amount to about $120 \times |\Xi|$ additional variables and constraints. While an even smaller reduced-space formulation than the used one is possible by eliminating the auxiliary variables A_{ACC}, p_{max}, P_F, $P_{F,nom}$, P_P, $P_{P,nom}$, K_S, $\dot{V}_{o,rel}$, Δh_{rel}, P_T, and $P_{T,nom}$, preliminary optimization results indicated that this does not improve computational time due to the resulting deterioration of relaxations.

To improve computational performance, we scaled all variables to a unit range and investigated different branching strategies. Compared to the default branching strategy, where all variables have branching priority 1, giving all design variables a higher priority of 2, 5, or 10 improves the performance somewhat, although the difference between choosing 5 and 10 is negligible. We found that a much better performance can be achieved by maintaining a priority 1 for the auxiliary variables mentioned above, whose value is determined by other variables or constraints, and setting the priority of all other variables to the heuristic value $1 + n^2$, where n is the number of functions each variable is present in.

3.1 Optimization for the average ambient temperature

Optimizing the system for any single ambient temperature results in a design that will generally be suboptimal, and may even be infeasible for other temperatures. To illustrate this point, we consider the optimization for a single operational scenario, corresponding to the weighted average of ambient temperatures from Fig. 6, i.e., $\Xi = \{\overline{T}_{amb}\}, \pi^{\overline{T}_{amb}} = 1$.

When fixing the optimal design decisions obtained for this average ambient temperature case, we can optimize the operational decisions for different ambient temperatures. For temperatures up to 15 °C MAiNGO finds a local optimum in preprocessing, and proves these local optima to be global within few seconds of branch and bound. The remaining 5 temperatures (cf. Fig. 6), however, are found to be infeasible within few seconds of branch and bound, also see Fig. 7. This is because the original optimization selects a design that is optimal for the average temperature but is operated at the boundary of the feasibility region for this temperature: The fans operate at their peak power and tube-side velocities for EVA and REC and shell-side velocities for ECO, REC, and SUP are at their maximum bounds for temperatures close to $\overline{T}_{amb}$. As long as the brine mass flow $\dot{m}_{br}$ is fixed to its maximum value, the states of the working fluid are constrained to remain identical for all ambient temperatures. If the velocity limits are relaxed and $\dot{m}_{br}$ is allowed to be reduced by making it an operational

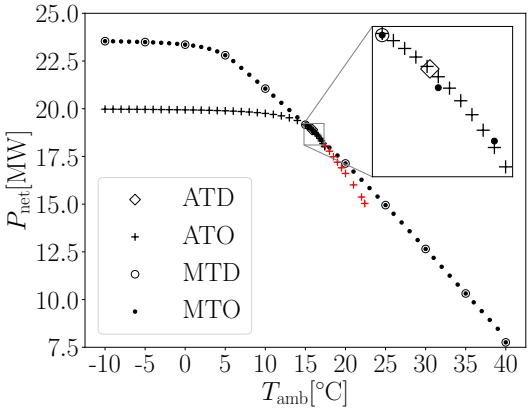

Fig. 7. Comparison of performance for the designs resulting from optimizations considering the average temperature only (ATD), or all 11 temperatures from Fig. 6 (MTD). The closeup shows that around the average temperature, the ATD slightly outperforms the MTD, however, running operational optimizations on a finer temperature resolution ($\leq 1\,\text{K}$) using the average (ATO) or multiple-temperature (MTO) design shows that the former is only feasible for a subset of all considered temperatures. When allowing for an increase in fluid speeds and a decrease in the brine mass flow, operation can be extended slightly (+). For ambient temperatures above 22.4 °C operation with the ATD is infeasible.

variable, additional feasible points can be found for higher ambient temperatures (red crosses in Fig. 7). For ambient temperatures above 22.4 °C, however, operational problems remain infeasible. Similarly, optimizing the system for any other single operating scenario, results in designs that only allow for feasible operation close to the respective temperature. For example, optimizing for the maximum expected ambient temperature results in a design that becomes infeasible for ambient temperatures below 0 °C as Re_{air} approaches the lower limit of the validity range for the use of the Ganguli correlation, see Eq. (60).

3.2 Comparing results for single and multiple operating points

The results from the previous section suggest that we might find a more robust system design via an optimization for a single ambient temperature if we artificially restrict operational constraints, in order to obtain a more conservative design that leaves room for the necessary variations in operating points during off-design. While this may in fact produce a design that is feasible for all ambient temperatures, it is not clear which constraints to relax or how to balance conservatism and optimality. A more straightforward approach is to directly consider multiple operating points in a single optimization problem, e.g., as done in Yunt et al. (2008). By assigning appropriate weights to the objective contributions of different operational scenarios, the optimizer will automatically select the design that produces the best results based on the weighted average, also compare Fig. 7. A particular benefit of the presented model is that no explicit characterization of design and off-design operation is necessary. Instead, the design is automatically adjusted by the optimizer to account for all considered operating points.

Fig. 8 shows a qualitative comparison of the optimal variable values resulting from optimizations considering a single ambient temperature, each (ST), and an optimization that considers multiple operating points, corresponding to the 11 temperatures shown in Fig. 6 (MT), each weighted by the respective likelihood. It can be seen that some design quantities are similar or even identical for all cases while for other quantities, very different values are optimal depending on the considered ambient temperature. Furthermore, while the optimal design of the MT optimization is close to the weighted average of the ST designs for most quantities, the optimal value from the MT optimization for $d_{\text{s,ECO}}$ is smaller and the $L_{\text{t,SUP}}/d_{\text{s,SUP}}$ and $L_{\text{B,ECO}}/d_{\text{s,ECO}}$ ratios are larger than in all ST cases. As with the optimal designs, the ranges of optimal operational values for the ST optimizations vary significantly for some of the variables. The solution of the MT optimization on the other hand exhibits approximately constant values for T_{amb} below 10 °C for all operational quantities, except for P_{F} and $\Delta T_{\text{min,ACC}}$.

Generally, feasibility for operational scenarios not considered during the optimization determining the system design cannot be guaranteed. However, for the present case study the monotonicity of operational variable values for the MT case in Fig. 8 suggests that the MT design might be feasible for all ambient temperatures from −10 to 40 °C. Indeed, when fixing the design variables to the values from the MT solution and optimizing the operational strategies for intermediate temperatures in steps of 1 K, MAiNGO finds feasible solutions in all cases, also see Fig. 7. This is in contrast to the optimal design from the ST optimization considering only $\overline{T}_{\text{amb}}$ (cf. Section 3.1), and demonstrates the

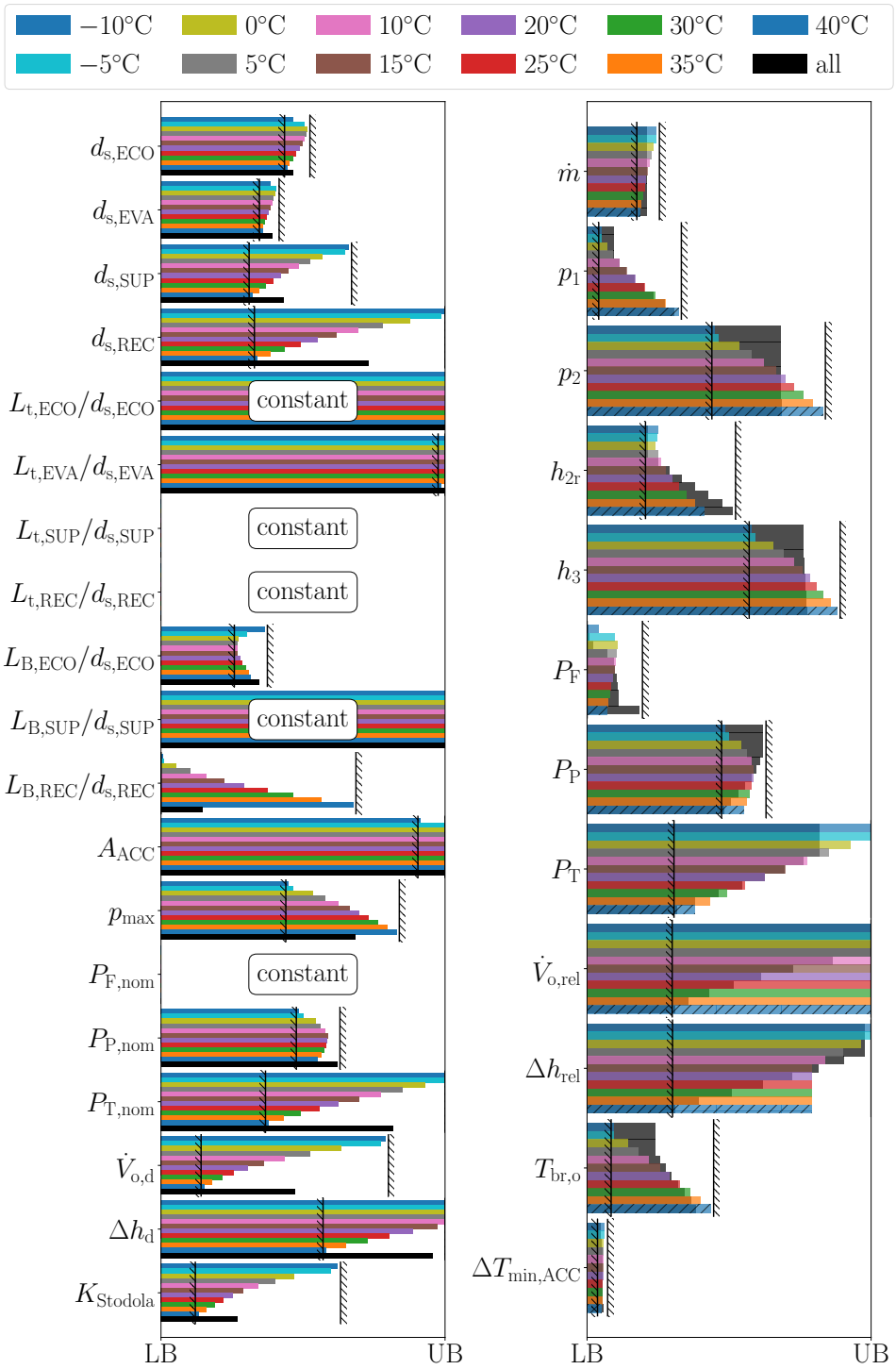

Fig. 8. Comparison of the variable ranges for single-temperature and multiple-temperature (all) optimizations, left: design, right: operation with results for single-temperature optimizations superimposed over those for the multiple-temperature optimization. A reduction of the considered variable ranges is proposed based on the results and indicated via hatched vertical lines (left hatch: new lower bound, right hatch: new upper bound). Design quantities for which the overall variation is less than 1% of the original range are considered constant, i.e., they are fixed to the value of the multiple-temperature optimization.

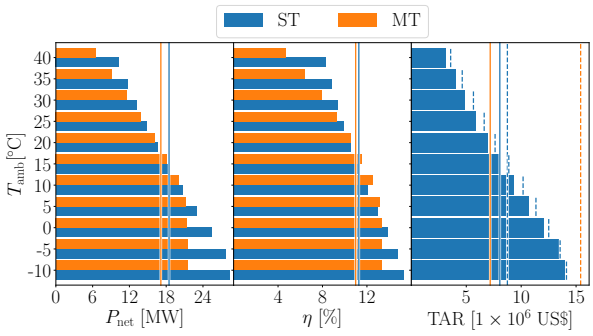

Fig. 9. Comparison of the net power P_{net}, total efficiency $\eta = P_{\text{net}}/\dot{Q}_{\text{br}}$, and TAR resulting from single-temperature (ST) and multiple-temperature (MT) optimizations. Solid vertical lines correspond to weighted averages, dashed vertical lines to upper bounds. The dashed blue line extending over the full height corresponds to the wait-and-see bound obtained by taking the weighted average of the ST bounds.

robustness of the proposed approach.

3.3 Global optimization with reduced variable ranges

Even after 24 h of CPU time, relative gaps for the ST optimizations are between 13 and 124 %, and that of the MT optimization is at 121%. As a result, it is not clear whether a significantly better design is possible. To obtain better bounds on the optimal objective value, we repeat the optimizations from the previous section with the reduced ranges shown in Fig. 8.

As before, MAiNGO does not improve the feasible point found during preprocessing for any of the considered optimizations. The design values corresponding to the best feasible point of the MT optimization are given in Tab. 5. For the ST optimizations, both net power and overall efficiency increase almost linearly with decreasing temperature until −5 °C. In contrast, the values from the MT solution reach a plateau for temperatures below 10 °C in both cases, and always lie below those of the ST optimizations, see Fig. 9.

A well-known result from the literature on two-stage stochastic programming (see, e.g., Madansky, 1960) is that the weighted average of the globally optimal objective value of so-called *wait-and-see subproblems* (where it is assumed that separate first-stage decisions may be taken for each scenario) is an optimistic bound to the optimal objective value for the *here-and-now problem* (where first-stage decisions need to be taken before the realization of uncertain parameters). In the context of the present work, the first-stage decisions are design decisions, the *wait-and-see problems* correspond to the ST design problems and the *here-and-now problem* corresponds to the MT problem. In lack of a globally optimal objective value, the upper bounds on the ST problems can be used to obtain the wait-and-see bound. In the following we show that within the same time-frame, this wait-and-see bound can be much tighter than the upper bound from the MT optimization.

After 24 h, the upper bound for the TAR obtained from the direct optimization of the MT problem (dashed orange line in the right plot in Fig. 9) is still 93% larger than the value for the best solution with a TAR of $7.81{\times}10^6\ \frac{\text{US\$}}{\text{a}}$ (solid orange line in the right plot in Fig. 9). In contrast, the bound obtained by taking the weighted average of the upper bounds from the ST optimizations (dashed blue line in the right plot in Fig. 9) is only 11% larger than the best found TAR. Note that while multiple ST optimizations are necessary to generate this wait-and-see bound, it does not necessarily take more time than generating the direct bound from the MT problem, as the ST problems (and the MT problem) may be solved in parallel on separate CPUs.

The solid blue vertical line in the right plot in Fig. 9 corresponds to the lowest possible bound we can hope to obtain using the wait-and-see approach. It would be obtained, if the bounds of the subproblems converged to the respective objective values of the best feasible solutions. Unlike the MT optimization, the wait-and-see-approach is therefore not guaranteed to converge. If no better feasible point is found, the best possible wait-and-see bound would result in a gap of 7%. It is however possible to improve the wait-and-see approach via a decomposition algorithm as has been done by, e.g., Cao and Zavala (2019).

4 Conclusion

We present a detailed model of an air-cooled geothermal ORC, simultaneously taking into account system design as well as operational decisions for multiple operational scenarios. Through the incorporation of ANNs as data-driven surrogate models, accurate working fluid properties as well as component characteristics are incorporated while maintaining computational tractability. We implement this model using our open-source modeling framework COMANDO and formulate a mathemat-

Tab. 5. Numerical results from the MT optimization. Top: geometry of the shell and tube exchangers, middle: remaining design variables, bottom: TAR and bounds (in million $\frac{\text{US\$}}{\text{a}}$). Note that baffle spacing for the evaporator is missing as it does not occur in the considered correlations.

HX	$d_{\text{s,HX}}$ [m]	$\frac{L_{\text{t,HX}}}{d_{\text{s,HX}}}$ [–]	$\frac{L_{\text{B,HX}}}{d_{\text{s,HX}}}$ [–]
ECO	1.43	12	0.4765
EVA	1.285	12	–
REC	1.959	4	0.3159
SUP	1.366	4	1

A_{ACC}	$P_{\text{c,nom}}$ [MW]			$\dot{V}_{\text{T,o,d}}$	$\Delta h_{\text{T,d}}$	K_{S}
[m^2]	F	P	T	$\left[\frac{\text{m}^3}{\text{s}}\right]$	$\left[\frac{\text{kJ}}{\text{kg}}\right]$	[cm^2]
1×10^6	0.037	1.28	12.44	24.13	62.66	20.83

TAR	wait-and-see bound	direct bound
7.81	8.70	15.1

ical programming problem, maximizing total annualized revenue. We solve several instances of this problem for different sets of operating scenarios, corresponding to single or multiple ambient temperatures using our open-source global optimization solver MAiNGO. If only a single temperature is considered, e.g., the average or maximum ambient temperature, we obtain a system design that enables optimal operation for that temperature, but becomes infeasible for temperatures that are far from the considered one. In contrast, considering multiple operating points along with their relative likelihood during the optimization results in a robust design that can be operated over the entire operating range and allows for an operation providing maximum expected total annualized revenue.

Our contribution is twofold: first, we demonstrate the importance of considering multiple operating points within design problems, instead of a single one. Second, we show that single-temperature optimizations can still provide valuable bounding information that can be used to improve the bound obtained from multiple-temperature optimization. For the present case study, we are able to reduce the upper bound on the total annualized return from 93% to 11%.

For improved computational efficiency, algorithms exploiting the special structure of simultaneous design and operation problems may also be employed, which is a topic for future research. Further research may relax simplifying assumptions made here, e.g., the restriction to a single stage turbine, or the neglection of pressure drops. Finally, considering the influence of additional variable operational quantities, e.g., the electricity price, could be of interest.

Nomenclature

Acronyms

ACC	air cooled condenser
ANN	artificial neural network
BOP	balance of plant
MT	multiple temperature
SQP	sequential quadratic programming
ST	single temperature

Subscripts

0	base cost
amb	ambient conditions
ann	annuitiy
b	boiling
B	baffle
br	geothermal brine
C	Colburn
c	cold / component
con	condensation
crit	critical point
cs	cross-section
D	Darcy
d	related to design state
e	entry
el	electricity
F	fan
f	fin
h	hot

HX	related to a heat exchanger
I	investment cost
i	inside, related to inlet state
ib	isobutane
is	related to isentropic outlet
m	mechanical
nb	nucleate boiling
op	operational
o	outside, related to outlet state
p	tube pitch
pinch	ACC pinch point (start of condensation)
R	fouling resistance
rel	relative to design value
sat	value at saturation
S&T	shell and tube
t	tube
tb	tube-bundle
tp	tube passes
w	wall
wf	weighted fin

Symbols

λ	heat conductivity [W/m/K]
α	fluid heat transfer coefficient [W/m^2/K]
η	efficiency [–]
A	area [m^2]
C	cost [US$]
k	thermal conductivity [W/m/K]
c_p	mass-specific heat capacity [J/kg/K]
d	diameter [m]
e	temperature effectiveness [–]
F	correction factor [–]
h	specific enthalpy [J/kg]
K_S	coefficient from Stodols's ellipse law [m^2]
L	length [m]
$\dot{m}$	mass flow rate [kg/s]
Nu	Nusselt number [–]
P	electrical power [W]
p	pressure [Pa]
PR	pressure ratio [–]
Pr	Prandtl number [–]
$\dot{Q}$	heat flow rate [W]
r	reduction coefficient for off-design according to Ghasemi et al. (2013a) $\frac{\eta}{\eta_{\mathrm{T,d}}}$ [–]
Re	Reynolds number [–]
Ξ	set of operational scenarios
ξ	operational scenario
SP	turbine size parameter $\frac{\dot{V}_{\mathrm{o,is,d}}^{0.5}}{\Delta h_{\mathrm{is,d}}^{0.25}}$ [m]
T	temperature [K]
t	thickness [m]
TAR	total annual return [US$/a]
U	overall heat transfer coefficient [W/m^2/K]
$\dot{V}$	volumetric flow rate [m^3/s]
v	velocity [m/s]
μ	kinematic viscosity [m/s^2]
VR	turbine volume ratio $\frac{\dot{V}_{\mathrm{o,is,d}}}{\dot{V}_{\mathrm{i,d}}}$ [–]
x	vapor quality [–]

References

S. Ahmad, B. Linnhoff, and R. Smith. Design of Multipass Heat Exchangers: An Alternative Approach. *J. Heat Transf.*, 110(2):304–309, 1988. doi:10.1115/1.3250484.

M. Astolfi, M. C. Romano, P. Bombarda, and E. Macchi. Binary ORC (organic Rankine cycles) power plants for the exploitation of medium–low temperature geothermal sources – Part A: Thermodynamic optimization. *Energy*, 66:423–434, Mar. 2014a. doi:10.1016/j.energy.2013.11.056.

M. Astolfi, M. C. Romano, P. Bombarda, and E. Macchi. Binary ORC (organic Rankine cycles) power plants for the exploitation of medium–low temperature geothermal sources – Part B: Techno-economic optimization. *Energy*, 66:435–446, Mar. 2014b. doi:10.1016/j.energy.2013.11.057.

M. Astolfi, L. N. L. Diega, M. C. Romano, U. Merlo, S. Filippini, and E. Macchi. Application of the Novel 'emeritus' Air Cooled Condenser in Geothermal ORC. *Energy Procedia*, 129:479–486, Sept. 2017. doi:10.1016/j.egypro.2017.09.164.

J. R. Birge and F. Louveaux. *Introduction to Stochastic Programming*. Springer Science & Business Media, 2011.

D. Bongartz, J. Najman, S. Sass, and A. Mitsos. MAiNGO: McCormick based Algorithm for mixed integer Nonlinear Global Optimization. Technical report, Process Systems Engineering (AVT. SVT), RWTH Aachen University, 2018. Available at https://www.avt.rwth-aachen.de/global/show_document.asp?id=aaaaaaaaabclahw, accessed 10 November 2021.

F. Calise, C. Capuozzo, A. Carotenuto, and L. Vanoli. Thermoeconomic Analysis and Off-design Performance of an Organic Rankine Cycle Powered by Medium-temperature Heat Sources. *Sol. Energy*, 103:595–609, 2014. doi:10.1016/j.solener.2013.09.031.

Y. Cao and V. M. Zavala. A Scalable Global Optimization Algorithm for Stochastic Nonlinear Programs. *J. Global Optim.*, 75(2):393–416, 2019. doi:10.1007/s10898-019-00769-y.

F. Capra and E. Martelli. Numerical Optimization of Combined Heat and Power Organic Rankine Cycles – Part B: Simultaneous Design & Part-load Optimization. *Energy*, 90:329–343, Oct. 2015. doi:10.1016/j.energy.2015.06.113.

D. Casartelli, M. Binotti, P. Silva, E. Macchi, E. Roccaro, and T. Passera. Power Block Off-design Control Strategies for Indirect Solar ORC Cycles. *Energy Procedia*, 69:1220–1230, May 2015. doi:10.1016/j.egypro.2015.03.166.

D. H. Cooke. On Prediction of Off-design Multistage Turbine Pressures by Stodola's Ellipse. In *1984 Joint Power Gener. Conf.: GT Papers*, Toronto, Canada, 1984. ASME. doi:10.1115/84-jpgc-gt-14.

L. da Lio, G. Manente, and A. Lazzaretto. Predicting the Optimum Design of Single Stage Axial Expanders in ORC Systems: Is There a Single Efficiency Map for Different Working Fluids? *Appl. Energy*, 167:44–58, Apr. 2016. doi:10.1016/j.apenergy.2016.01.020.

R. S. El-Emam and I. Dincer. Exergy and Exergoeconomic Analyses and Optimization of Geothermal Organic Rankine Cycle. *Appl. Therm. Eng.*, 59(1-2):435–444, Sept. 2013. doi:10.1016/j.applthermaleng.2013.06.005.

A. Erdogan, C. O. Colpan, and D. M. Cakici. Thermal Design and Analysis of a Shell and Tube Heat Exchanger Integrating a Geothermal Based Organic Rankine Cycle and Parabolic Trough Solar Collectors. *Renew. Energy*, 109:372–391, Aug. 2017. doi:10.1016/j.renene.2017.03.037.

A. Ganguli, S. S. Tung, and J. Taborek. Parametric Study of Air-cooled Heat Exchanger Finned Tube Geometry. In *AIChE symp. ser.*, volume 81, pages 122–128, Denver, CO, 1985. 245.

H. Ghasemi, M. Paci, A. Tizzanini, and A. Mitsos. Modeling and Optimization of a Binary Geothermal Power Plant. *Energy*, 50:412–428, Feb. 2013a. doi:10.1016/j.energy.2012.10.039.

H. Ghasemi, M. Paci, A. Tizzanini, and A. Mitsos. Modeling and Optimization of a Binary Geothermal Power Plant. Preprint, available at http://hdl.handle.net/1721.1/104031, accessed 10 November 2021, 2013b.

H. Ghasemi, A. Tizzanini, M. Paci, and A. Mitsos. Optimization of Binary Geothermal Power Systems. In *Comput. Aided Chem. Eng.*, volume 32, pages 391–396. Elsevier, 2013c. doi:10.1016/b978-0-444-63234-0.50066-x.

V. Gnielinski. New Equations for Heat and Mass Transfer in Turbulent Pipe and Channel Flow. *Int. Chem. Eng.*, 16(2):359–368, 1976.

V. Gnielinski. *Forced Convection in Ducts*, volume 1, page 5. Hemisphere Washington, DC, 1983.

S. L. Gómez-Aláez, V. Brizzi, D. Alfani, P. Silva, A. Giostri, and M. Astolfi. Off-design Study of a Waste Heat Recovery ORC Module in Gas Pipelines Recompression Station. *Energy Procedia*, 129:567–574, Sept. 2017. doi:10.1016/j.egypro.2017.09.205.

B. Grimstad and H. Andersson. ReLU networks as surrogate models in mixed-integer linear programs. *Computers & Chemical Engineering*, 131:106580, dec 2019. doi:10.1016/j.compchemeng.2019.106580.

J. Hernandez-Galan and L. A. Plauchu. Determination of fouling factors for shell-and-tube type heat exchangers exposed to Los Azufres geothermal fluids. *Geothermics*, 18(1-2):121–128, 1989. doi:10.1016/0375-6505(89)90018-7.

W. R. Huster, A. M. Schweidtmann, and A. Mitsos. Impact of Accurate Working Fluid Properties on the Globally Optimal Design of an Organic Rankine Cycle. *Comput. Aided Chem. Eng.*, 47:427–432, 2019. doi:10.1016/b978-0-12-818597-1.50068-0.

W. R. Huster, A. M. Schweidtmann, J. T. Lüthje, and A. Mitsos. Deterministic Global Superstructure-based Optimization of an Organic Rankine Cycle. *Comput. Chem. Eng.*, 141:106996, Oct. 2020a. doi:10.1016/j.compchemeng.2020.106996.

W. R. Huster, A. M. Schweidtmann, and A. Mitsos. Globally Optimal Working Fluid Mixture Composition for Geothermal Power Cycles. *Energy*, 212:118731, Dec. 2020b. doi:10.1016/j.energy.2020.118731.

W. R. Huster, A. M. Schweidtmann, and A. Mitsos. Hybrid Mechanistic Data-driven Modeling for the Deterministic Global Optimization of a Transcritical Organic Rankine Cycle. In *Comput. Aided Chem. Eng.*, volume 48, pages 1765–1770. Elsevier, 2020c. doi:10.1016/b978-0-12-823377-1.50295-0.

M. Kalikatzarakis and C. A. Frangopoulos. Thermo-economic Optimization of Synthesis, Design and Operation of a Marine Organic Rankine Cycle System. *Proc. IMechE, Part M: J. Eng. Marit. Environ.*, 231(1):137–152, 2016. doi:10.1177/1475090215627179.

P. Kall and S. W. Wallace. *Stochastic Programming*. John Wiley and Sons Ltd, 1994. ISBN 9780471951087.

U. Kaplan, R. Sfar, and Y. Shilon. Small Scale Geothermal Power Plants with Less Than 5.0 Mw Capacity. *Bull. Hydrogéol*, 17:433–440, 1999.

D. Q. Kern and A. D. Kraus. *Extended Surface Heat Transfer*. McGraw-Hill, 1972. ISBN 0070341958.

T. Kuppan. *Heat Exchanger Design Handbook*. CRC Press, May 2013. doi:10.1201/b14877.

G. Kyriakarakos, E. Ntavou, and D. Manolakos. Investigation of the Use of Low Temperature Geothermal Organic Rankine Cycle Engine in an Autonomous Polygeneration Microgrid. *Sustainability*, 12(24):10475, 2020. doi:10.3390/su122410475.

M. Lampe, M. Stavrou, H. M. Bücker, J. Gross, and A. Bardow. Simultaneous Optimization of Working Fluid and Process for Organic Rankine Cycles Using PC-SAFT. *Ind. Eng. Chem. Res.*, 53(21): 8821–8830, May 2014. doi:10.1021/ie5006542.

M. Langiu, D. Y. Shu, F. J. Baader, D. Hering, U. Bau, A. Xhonneux, D. Müller, A. Bardow, A. Mitsos, and M. Dahmen. COMANDO: A Next-Generation Open-Source Framework for Energy Systems Optimization. *Comput. Chem. Eng.*, page 107366, May 2021. doi:10.1016/j.compchemeng.2021.107366.

A. Lazzaretto and G. Manente. A New Criterion to Optimize ORC Design Performance Using Efficiency Correlations for Axial and Radial Turbines. *Int. J. Thermodyn.*, 17(3):192, Sept. 2014. doi:10.5541/ijot.562.

I. Lee, J. W. Tester, and F. You. Systems analysis, design, and optimization of geothermal energy systems for power production and polygeneration: State-of-the-art and future challenges. *Renewable and Sustainable Energy Reviews*, 109: 551–577, 2019. doi:10.1016/j.rser.2019.04.058.

L. Liu, T. Zhu, N. Gao, and Z. Gan. A Review of Modeling Approaches and Tools for the Off-design Simulation of Organic Rankine Cycle. *J. Therm. Sci.*, 27(4):305–320, June 2018. doi:10.1007/s11630-018-1023-2.

L. Lueg, B. Grimstad, A. Mitsos, and A. M. Schweidtmann. reluMIP: Open Source Tool for MILP Optimization of ReLU Neural Networks, 2021. URL `https://github.com/ChemEngAI/ReLU_ANN_MILP`.

E. Macchi. The Choice of Working Fluid: The Most Important Step for a Successful Organic Rankine Cycle (and an Efficient Turbine). In *2nd Int. Seminar ORC Power Syst.*, pages 7–8, Rotterdam, The Netherlands, 10 2013.

E. Macchi and M. Astolfi. *Organic Rankine Cycle (ORC) Power Systems: Technologies and Applications*, chapter Axial Flow Turbines for Organic Rankine Cycle Applications, pages 299–319. Elsevier, 2017a. doi:10.1016/b978-0-08-100510-1.00009-0.

E. Macchi and M. Astolfi. *Organic Rankine Cycle (ORC) Power Systems: Technologies and Applications*. Elsevier, 2017b. doi:10.1016/c2014-0-04239-6.

E. Macchi and A. Perdichizzi. Efficiency Prediction for Axial-flow Turbines Operating with Nonconventional Fluids. *J. Eng. P.*, 103(4):718–724, Oct. 1981. doi:10.1115/1.3230794.

A. Madansky. Inequalities for Stochastic Linear Programming Problems. *Manag. Sci.*, 6(2):197–204, 1960. doi:10.1287/mnsc.6.2.197.

P. J. Mago, L. M. Chamra, K. Srinivasan, and C. Somayaji. An Examination of Regenerative Organic Rankine Cycles Using Dry Fluids. *Appl. Therm. Eng.*, 28(8-9):998–1007, 2008. doi:10.1016/j.applthermaleng.2007.06.025.

G. Manente, A. Toffolo, A. Lazzaretto, and M. Paci. An Organic Rankine Cycle Off-design Model for the Search of the Optimal Control Strategy. *Energy*, 58:97–106, Sept. 2013. doi:10.1016/j.energy.2012.12.035.

E. Martelli and E. Amaldi. PGS-COM: A hybrid method for constrained non-smooth black-box optimization problems: Brief review, novel algorithm and comparative evaluation. *Comput. Chem. Eng.*, 63:108–139, 2014. doi:10.1016/j.compchemeng.2013.12.014.

E. Martelli, F. Capra, and S. Consonni. Numerical Optimization of Combined Heat and Power Organic Rankine Cycles – Part a: Design Optimization. *Energy*, 90:310–328, Oct. 2015. doi:10.1016/j.energy.2015.06.111.

N. Mazzi, S. Rech, and A. Lazzaretto. Off-design Dynamic Model of a Real Organic Rankine Cycle System Fuelled by Exhaust Gases from Industrial Processes. *Energy*, 90:537–551, Oct. 2015. doi:10.1016/j.energy.2015.07.083.

A. Meroni, A. L. Seta, J. Andreasen, L. Pierobon, G. Persico, and F. Haglind. Combined Turbine and Cycle Optimization for Organic Rankine Cycle Power Systems—part a: Turbine Model. *Energies*, 9(5):313, Apr. 2016. doi:10.3390/en9050313.

G. L. Mines and D. S. Wendt. Air-Cooled Condensers for Next Generation Geothermal Power Plants: Final Report. Technical report, Idaho National Laboratory (INL), 2013.

M. Mistry and R. Misener. Optimising Heat Exchanger Network Synthesis Using Convexity Properties of the Logarithmic Mean Temperature Difference. *Comput. Chem. Eng.*, 94:1–17, 2016. doi:10.1016/j.compchemeng.2016.07.001.

J. Najman and A. Mitsos. Convergence Order of McCormick Relaxations of LMTD Function in Heat Exchanger Networks. *Comput. Aided Chem. Eng.*, 38:1605–1610, 2016. doi:10.1016/b978-0-444-63428-3.50272-1.

H. Nazif. Feasibility of Developing Binary Power Plants in the Existing Geothermal Production Areas in Indonesia. *United Nations University Geothermal Training Programme, Reykjavik, Iceland*, pages 709–735, 2011.

Y. Nusiaputra, H.-J. Wiemer, and D. Kuhn. Thermal-economic Modularization of Small, Organic Rankine Cycle Power Plants for Mid-enthalpy Geothermal Fields. *Energies*, 7(7):4221–4240, July 2014. doi:10.3390/en7074221.

L. Pierobon, T.-V. Nguyen, U. Larsen, F. Haglind, and B. Elmegaard. Multi-objective Optimization of Organic Rankine Cycles for Waste Heat Recovery: Application in an Offshore Platform. *Energy*, 58:538–549, Sept. 2013. doi:10.1016/j.energy.2013.05.039.

R. Pili, A. Romagnoli, H. Spliethoff, and C. Wieland. Techno-economic Analysis of Waste Heat Recovery with ORC from Fluctuating Industrial Sources. *Energy Procedia*, 129:503–510, Sept. 2017. doi:10.1016/j.egypro.2017.09.170.

R. Pili, A. Romagnoli, M. Jiménez-Arreola, H. Spliethoff, and C. Wieland. Simulation of Organic Rankine Cycle – Quasi-steady State Vs Dynamic Approach for Optimal Economic Performance. *Energy*, 167:619–640, Jan. 2019a. doi:10.1016/j.energy.2018.10.166.

R. Pili, N. Siamisiis, R. Agromayor, L. O. Nord, C. Wieland, and H. Spliethoff. Efficiency Correlations for Off-design Performance Prediction of Orc Axial-flow Turbines. In *5th Int. Seminar ORC Power Syst.*, Athens, Greece, 2019b. The National Technical University of Athens (NTUA) Athens, Greece.

R. Pili, H. Spliethoff, and C. Wieland. Effect of Cold Source Conditions on the Design and Control of Organic Rankine Cycles for Waste Heat Recovery from Industrial Processes. In *32nd ECOS*, 2019c.

B. Saleh, G. Koglbauer, M. Wendland, and J. Fischer. Working Fluids for Low-temperature Organic Rankine Cycles. *Energy*, 32(7):1210–1221, 2007. doi:10.1016/j.energy.2006.07.001.

H. Schedwill. Thermische Auslegung von Kreuzstromwärmeaustauschern. Fortschr-Ber. *VDI Zeitschrift*, 6(19), 1968.

J. Schilling, M. Lampe, J. Gross, and A. Bardow. Working Fluid Selection for Organic Rankine Cycles Based on Continuous-molecular Targets. In *ASME ORC 2015 - 3rd Int. Semin. ORC Power Syst.*, volume 1, pages 732–741, Brussels, Belgium, 2015.

J. Schilling, M. Lampe, J. Gross, and A. Bardow. 1-stage CoMT-CAMD: An Approach for Integrated Design of ORC Process and Working Fluid Using PC-SAFT. *Chem. Eng. Sci.*, 159:217–230, 2017. doi:10.1016/j.ces.2016.04.048.

A. M. Schweidtmann and A. Mitsos. Deterministic Global Optimization with Artificial Neural Networks Embedded. *J. Optim. Theory Appl.*, 189:925–948, Oct. 2018. doi:10.1007/s10957-018-1396-0.

A. M. Schweidtmann, W. R. Huster, J. T. Lüthje, and A. Mitsos. Deterministic Global Process Optimization: Accurate (single-species) Properties Via Artificial Neural Networks. *Comput. Chem. Eng.*, 121:67–74, Feb. 2019. doi:10.1016/j.compchemeng.2018.10.007.

R. W. Serth. *Process Heat Transfer: Principles and Applications*. Elsevier, 2007. doi:10.1016/b978-0-12-373588-1.x5000-1.

A. L. Seta, A. Meroni, J. Andreasen, L. Pierobon, G. Persico, and F. Haglind. Combined Turbine and Cycle Optimization for Organic Rankine Cycle Power Systems—part B: Application on a Case Study. *Energies*, 9(6):393, May 2016. doi:10.3390/en9060393.

M. M. Shah. A General Correlation for Heat Transfer during Film Condensation inside Pipes. *Int. J. Heat Mass Transf.*, 22(4):547–556, Apr. 1979. doi:10.1016/0017-9310(79)90058-9.

M. M. Shah. An Improved and Extended General Correlation for Heat Transfer during Condensation in Plain Tubes. *HVAC&R Research*, 15(5):889–913, Sept. 2009. doi:10.1080/10789669.2009.10390871.

R. Smith. *Chemical Process: Design and Integration*. John Wiley & Sons, 2005.

J. Song, P. Loo, J. Teo, and C. N. Markides. Thermo-economic Optimization of Organic Rankine Cycle (ORC) Systems for Geothermal Power Generation: A Comparative Study of System Configurations. *Front. Energy Res.*, 8, 2020. doi:10.3389/fenrg.2020.00006.

T. Tartière and M. Astolfi. A World Overview of the Organic Rankine Cycle Market. *Energy Procedia*, 129:2–9, Sept. 2017. doi:10.1016/j.egypro.2017.09.159.

R. Turton, J. A. Shaeiwitz, D. Bhattacharyya, and W. B. Whiting. *Analysis, Synthesis and Design of Chemical Processes*. Prentice Hall, 2018. ISBN 0134177401.

M. Yunt, B. Chachuat, A. Mitsos, and P. I. Barton. Designing man-portable power generation systems for varying power demand. *AIChE J.*, 54(5):1254–1269, 2008. doi:10.1002/aic.11442.